CLIMATE PROFILING OF HYDROCARBON-BASED WORKING FLUIDS FOR ORGANIC RANKINE CYCLES

A Thesis

by

DEBRANJAN DAS

Submitted to the Graduate and Professional School of
Texas A&M University
in partial fulfillment of the requirements for the degree of

MASTER OF SCIENCE

Chair of Committee,	Reza Sadr
Co-Chair of Committee,	Michael Pate
Committee Members,	Jorge Alvarado
Head of Department,	Guillermo Aguilar

December 2021

Major Subject: Mechanical Engineering

ABSTRACT

This study selects a working fluid operating in an organic Rankine cycle at various climatic conditions for a number of major cities in the United States. Energy and exergy analyses are conducted for the cycle operating using a low-grade waste heat-source. Hydrocarbons are considered as working fluids based on their environmental and cycle performance characteristics. First law efficiency, dimensionless exergy-destruction in the evaporator, second law efficiency, and the volume power coefficient of the cycle are analyzed for different cycle operating pressures, heat-sink temperatures, and heat-source inlet temperatures for a constant turbine-work output. The average annual temperature of cities in the United States is considered as the heat-sink temperature. The system parameters for the working fluids are calculated at different pressure and source inlet temperatures from 400 K to 500 K. A rank-matrix with appropriate weights for each parameter is employed to select the optimal working fluid and the cycle operating pressure. After consideration of the environmental impact and the rank-matrix method of working fluid selection, dimethyl ether was found to be the most promising working fluid for heat-source inlet temperatures of 400 K and 450 K. In comparison, diethyl ether is a better working-fluid prospect for a heat-source temperature of 500 K. The optimal mode of cycle operation was also selected for various heat-source inlet temperatures; subcritical operation is preferred at 400 K, while a supercritical operation is preferred for 450 K and 500 K. The evaporator pressure corresponding to the best performance for each heat-

source temperature is achieved at 4298±52 kPa and 6803±93 kPa for dimethyl ether at 400 K and 450 K, respectively, and 5226±85 kPa for diethyl ether at 500 K.

DEDICATION

This thesis work is dedicated to my undergraduate sweetheart, Ms. Ananya Bothra, who has been my most significant source of encouragement and envisioned my graduation from one of the best colleges in the world. I am thankful for having you always by my side.

This work is also dedicated to my father, Mr. Debashish Das, a first-generation mechanical engineer and a veteran of the Indian Air Force, who has always been out there for me. He has always believed in me and provided me with the ideals and values to be a moral being.

Lastly, this work owes dedication to my mother, Mrs. Ranjana Das. Words would fall short for her great deeds in my life so that I will leave only my gratitude.

ACKNOWLEDGEMENTS

I would like to thank my committee chair, Dr. Sadr, my committee co-chair, Dr. Michael Pate, and my committee member, Dr. Jorge Alvarado, for their guidance and support throughout this research.

I would also like to thank Mr. Mohammad Kazim and his significant contribution to this work. Thanks to my friends and colleagues and the department faculty and staff for making my time at Texas A&M University a great experience. Thanks to Dr. Somnath Chakrabarti, my undergraduate thesis committee chair, for his constant support and best wishes.

I would also take this opportunity to especially thank Indrani Roy, Swagata Banerjee, Hitaishi Majumder, Ajinkya Raut, Prerana Bothra, and all those who have stood beside me in this graduate journey at Texas A&M, both in the United States and back in India.

CONTRIBUTORS AND FUNDING SOURCES

This work was supervised by a thesis committee consisting of Professor Reza Sadr, Professor Michael Pate, Professor Bryan Rasmussen of the Department of Mechanical Engineering, and Professor Jorge Alvarado of Engineering Technology & Industrial Distribution.

This work received assistance from Mohammad Kazim, a graduate student in the Department of Mechanical Engineering, and co-authored the journal article on the preliminary study. The work received technical (programming), grammatical and spelling checks from Ananya Bothra, a graduate student in the Department of Computer Science. This work was finally checked for a technical and general overview before submission by Dr. Reza Sadr and Dr. Michael Pate.

This work received no direct financial support or grants for completion. The J. Mike Walker ’66 Department of Mechanical Engineering presented a continuing student fellowship, Byron Anderson ’54 Fellowship, amounting to $1000, endowing a non-resident tuition waiver for the 2020-2021 academic year upon the nomination recommendation from Dr. Michael Pate. The research received support from Dr. Reza Sadr and Dr. Michael Pate, with positions of Student Technicians being awarded in the Summer of 2020 and 2021, respectively. The Department of Chemistry at Texas A&M provided a Graduate Assistant Teaching position for the Fall 2020 and Spring 2021 semesters.

NOMENCLATURE

ASHRAE	American Society of Heating, Refrigerating, and Air-Conditioning Engineers
CFC	Chlorofluorocarbon
CO_2	Carbon Dioxide
DEE	Diethyl Ether
DME	Dimethyl Ether
EES	Engineering Equation Solver
EPA	Environmental Protection Agency
XD	Exergy-destruction Rate (kW)
ex	Exergy of state point (kJ/kg)
GWP	Global Warming Potential
Q	Heat flow (kW)
HC	Hydrocarbon
HCFC	Hydrochlorofluorocarbon
m	Mass flow rate (kg/s)
NFP	No Flame Propagation
NIST	National Institute of Standards and Technology
ODP	Ozone Depletion Potential
ORC	Organic Rankine Cycle
W	Power (kW)

P	Pressure (kPa)
REFPROP	Reference Fluid Thermodynamic and Transport Properties
h	Specific enthalpy (kJ/kg)
s	Specific entropy (kJ/kg-K)
SORC	Supercritical Organic Rankine Cycle
T	Temperature (K)
U.S.	United States
VPC	Volume Power Coefficient
VRC	Volume Refrigeration Capacity
WF	Working Fluid
ZM	Zeotropic Mixture

Greek Alphabets

λ	Dimensionless exergy-destruction of the evaporator
η	First law efficiency (%)
θ	Reduced pressure
η_2	Second law efficiency (%)

TABLE OF CONTENTS

Page

LIST OF FIGURES

Page

LIST OF TABLES

Page

1. INTRODUCTION

The Rankine cycle has been the cornerstone of power generation ever since its invention in the mid-nineteenth century. This cycle efficiently generates electrical or mechanical energy from the heat by using working-fluid phase changes (mostly water). Over the centuries, the cycle has undergone significant modifications to improve its efficiency and application for specific conditions, e.g., regeneration and reheat. In the mid-twentieth century, Lucien Bronicki and Harry Zvi Tabor suggested that low-temperature heat can also be converted into useful work and electricity, leading to the birth of organic Rankine cycles [1].

1.1. Background

An organic Rankine cycle (ORC) is a Rankine cycle in which an organic fluid (pentane, propane, etc.) is used as a working fluid (WF) in place of water and steam. ORC is one of the most common methods used to extract valuable work from low-temperature heat-sources. According to the United States Department of Energy, low-temperature heat is temperature sources below 230 °C (or 500 K) and enlists ORC as a standard recovery technology for this temperature range [2]. The primary source of low-temperature sources for which ORCs are generally employed is geothermal, solar, industrial waste heat, internal combustion engines, and biomass [3][4].

The ORC has four essential components similar to the Rankine cycle: the evaporator (or boiler), turbine (or expander), condenser, and pump, as shown in Figure 1. The WF of the cycle enters the pump at state point 1 as a saturated-liquid, where the pressure is increased,

and the WF is fed to the evaporator at the compressed liquid state at state point 2. The low-temperature heat-source flows from point 5 through 6, transferring the heat energy to the cycle in the evaporator. The WF undergoes a phase change and enters the turbine at high pressure and high temperature. The WF undergoes expansion in the turbine, where the heat is converted into mechanical energy and then into electrical power with the use of a generator. The WF leaves the turbine at a saturated-vapor condition at state point 4 and enters the condenser. Heat is rejected from the cycle to the heat-sink at state points 7 through 8. At the condenser outlet, state point 1, the saturated-liquid is fed to the pump.

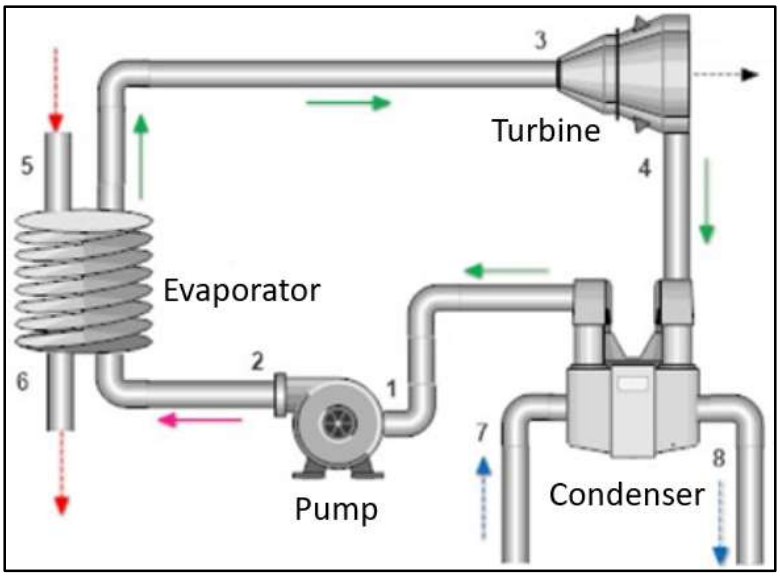

Figure 1. Schematics of organic Rankine cycle

Like the Rankine cycle, there is a phase change in the WF from a compressed liquid to a superheated vapor in a typical ORC. There are exergy losses due to the existing temperature change within the boilers that cycle operation can mitigate at the supercritical condition and replace the boiler with an evaporator. An ORC operating at supercritical

conditions is commonly referred to as a supercritical organic Rankine cycle (SORC). The WF in this cycle is heated directly from the saturated-liquid state into the supercritical state, bypassing the dome, which allows cycle to have a better thermal match with the heat-source points (7→8), minimizing the exergy loss, as shown in Figure 2. Also, by avoiding the boiling process typical in a boiler, the heating system's configuration is potentially simplified from a boiler to an evaporator [3]. The T-s diagram for both ORC and SORC is shown in Figure 2, corresponding to the state points in Figure 1.

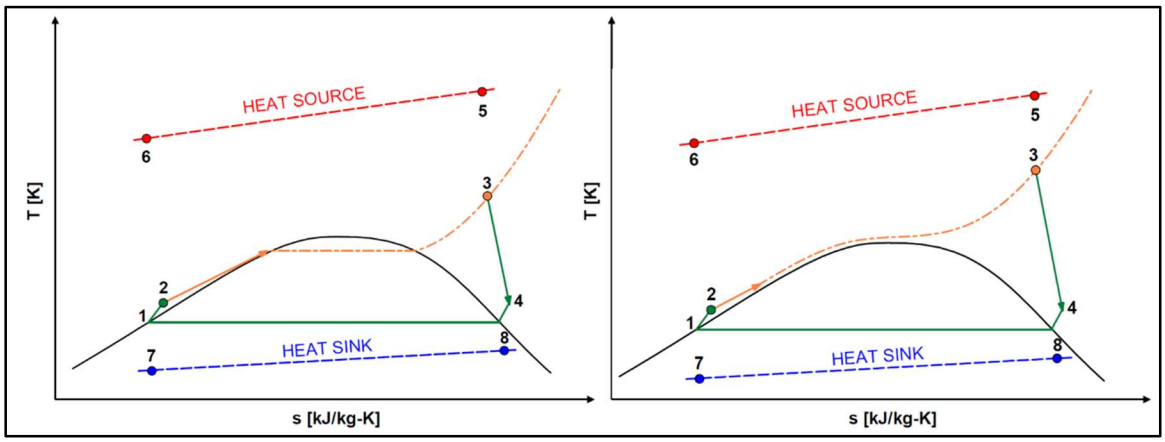

Figure 2. T-s diagram for organic Rankine cycle (left), and supercritical organic Rankine cycle (right)

When a zeotropic mixture (ZM) is used as the WF in the ORC and SORC, there is a further reduction in the exergy losses compared to the use of a pure WF. Heat rejection points (4→1) is not an isobaric process anymore, leading to better temperature matches and hence less exergy-destruction. The T-s diagram for both the ORC and SORC working with a ZM is shown in Figure 3, corresponding to the state points in Figure 1.

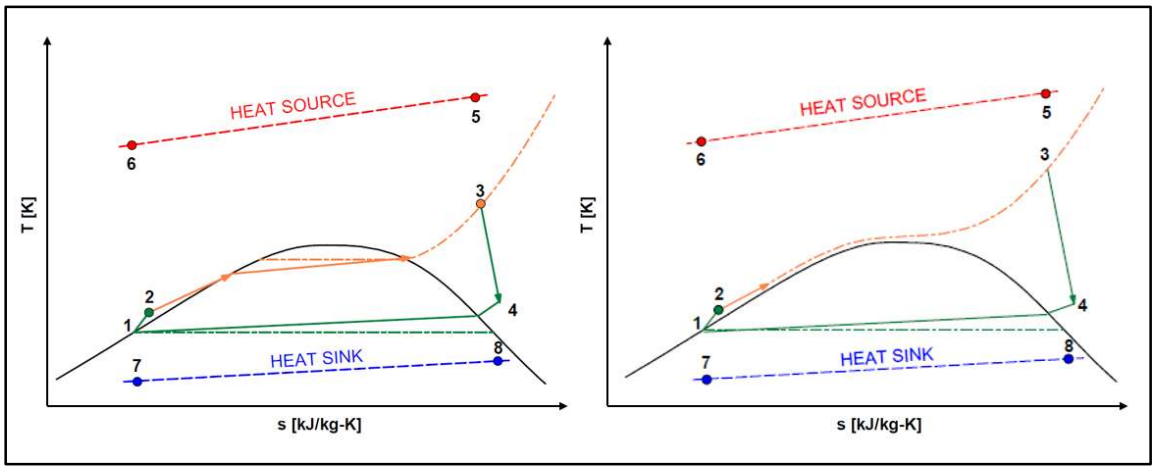

Figure 3. T-s diagram for organic Rankine cycle (left), and supercritical organic Rankine cycle (right) for zeotropic mixtures

1.2. Literature Review

The choice of the WF dramatically influences the performance of a power cycle. The Rankine cycle's wide popularity for power generation is attributed to the use of water as the WF. Similarly, for an ORC, the choice of a WF is pivotal to the efficient operation, which is attributed to cycle efficiency, system sizing, and other parameters. Sarkar [3] has reviewed carbon dioxide's applicability as the WF for SORC and states its supremacy over both steam and ORCs for low-grade heat conversion. The study highlights the better temperature match of the heat-source and WF when using carbon dioxide (CO_2).

The performance of twenty-three WFs for a subcritical ORC and SORC with a primary focus on the cycle thermal efficiency and net power output was analyzed by Javanshir *et al.* [4]. This study shows that thermal efficiency increases as the maximum pressure increases until the fluid's critical pressure is reached, after which the thermal efficiency is independent of maximum pressure. They categorized the WF into three types

and suggested using isentropic fluids (like trichlorofluoromethane, dichlorodifluoromethane, etc. with almost vertical saturation-vapor curves on a T-s diagram [5]) as the efficiency is independent of the turbine inlet temperature. They also presented an analysis of the supercritical cycle thermal efficiency under the different operating conditions as a function of dimensionless temperature.

Karellas *et al.* [6] investigated ORCs operating on waste heat-sources like geothermal, biomass, and internal combustion engines. Their work focused on the ORC's future in choosing the correct WF and the WF's thermodynamic properties in order to optimize the system's power output and efficiency. They presented the superiority of the supercritical cycle over the subcritical operation in thermodynamic efficiency for the same working conditions and WFs.

Mikielewicz *et al.* [7] investigated the performance of six organic fluids to be utilized at supercritical conditions in an ORC. They defined a dimensionless Jakob number to determine the system's efficiency at subcritical and supercritical conditions. Based on the analysis, they selected R141b and ethanol as their WF. Embarking on ORC's future, they have highlighted the efficiency and equipment sizing to be critical. Javanshir *et al.* [4] have also shown a superheated subcritical ORC, and the thermal efficiency is expressed as a function of the Jakob number.

Gao *et al.* [8] investigated eighteen organic WFs' performance in SORC. The WF selection in this study was based on cycle parameters like net power output, exergy-efficiency, expander size parameter, and heat exchanger requirement of the evaporator and the condenser. Based on the analysis, they selected R152a and R143a, and showed that

increasing the expander inlet temperature improves the net power output and the exergy-efficiency. The study highlights the inclusion of thermal stability of WFs at high temperatures and pressure in the future.

Vidhi *et al.* [9] presented the performance analysis of seven organic WFs in a SORC and they found R134a, that has an efficiency of 21% for a 200 °C geothermal source. The study included the cycle's efficiency for fixed and variable pressure ratios, and the selection criteria included the energy and exergy-efficiency. Two important conclusions were the importance of the optimum pressure ratio and the impact of higher condensation temperature.

Vetter *et al.* [10] studied the subcritical and supercritical operation of the ORC for a geothermal heat-source at 150 °C using 12 organic fluids. They considered specific net power, thermal efficiency, and heat input as parameters for WF selection. The study identified R143a and propane as suitable WFs for this operating condition. They suggested that the heat-source temperature and critical temperature of WF should be criteria for selecting WF.

Wang *et al.* [11] analyzed and selected WFs based on net power output, specific net power output, thermal efficiency, exergy-efficiency, flammability, safety, and environmental impact. In their study, the WF operates at subcritical, superheated, and supercritical cycles, and they have employed supercritical CO_2 to transfer heat from the geothermal heat-source to the cycle. The study analyzed thirty potential WFs and found the suitable one according to the ORC's operating state.

Mudasar *et al.* [12] investigated the performance of toluene operating in the ORC with heat from biogas combustion. They analyzed the toluene's performance based on fifteen cycle conditions and shortlisted the best seven working conditions. They finally suggested that the source temperature should be close to the critical temperature of WF and recommended the temperature difference be below 37 $°C$.

Quoilin *et al.* [13] provided a market review of the ORC and included cost figures for several commercial ORC modules and manufacturers. The study's analysis states the selection of WF and the expansion device as the significant technical challenges that need to be considered in the future. They reflected upon the impact of the WF on the system cost or on the component size as important research areas that can greatly augment the performance of an ORC. They also concluded that ZM and multiple evaporation pressures are the most promising research avenues with scope for performance improvement of up to 16%.

Ozdil *et al.* [14] carried out an extensive energy and exergy analysis of the ORC with a waste heat-source. They concluded that the evaporator has the highest entropy generation, as well as the highest exergy-destruction among all cycle components. The study also found that as the pinch-point decreases, exergy-destruction decreases; as the exergy-destruction decreases, the exergy-efficiency increases. Additionally, they suggested that the quality of fluid entering the evaporator should be as close to zero as possible, and the pinch-point temperature difference with the evaporation temperature should be less than 5.9 $°C$ to improve the performance of the ORC.

As pointed out by Ozdil *et al.* [14], pure working fluids have good cycle characteristics compared to mixtures; however, they tend to have a high degree of exergy-destruction due to pinch-point temperature difference. Also, binary mixtures are helpful due to their temperature matching characteristics with high heat-source temperatures. Sarkar [3] found that a ZM of CO_2 and Hydrocarbon (HC) blend is advantageous in terms of component size, flammability, net power, and efficiency.

A study by Deethayat *et al.* [15] showed an increase in the exergy-efficiency of an ORC with ZMs. Additionally, they developed a set of correlations to estimate the system's first and second law efficiency and the effectiveness of the internal heat exchanger for an ORC R245fa/ R152a ZM. The analysis showed that at a 80% mass fraction composition, the irreversibilities of R245fa were nearly steady. Also, the results showed that the temperature gliding during the phase change of the mixture could decrease irreversibilities at the evaporator and the cycle's condenser. Finally, the study highlighted the performance of the zeotropic blend and advocates its advantage in reducing the irreversibility.

Wang *et al.* [16] worked on machine learning algorithms for the performance prediction of ORCs by establishing a cycle database with thermodynamic modeling of four ORC configurations and seven WFs. Back propagation neural network and supports vector regression prediction models were built by predicting the database's error analysis. They concluded that considering accuracy, calculation time, economic cost, and safety, the ORC prediction and optimization method provides a new perspective for this research field. Rodrigues *et al.* [17] proposed a geographical information system-based model for

generating 5 MW power by utilizing ORC operating on produced biomass as the waste heat-source.

The study reported herein investigates the potential performance of HCs and other organic fluids as WFs in an ORC, possessing environmental benefits (low global warming and ozone depletion potential) and superior performance. Also, the focus on geographical profiling of WF selection for ORC herein is a novel approach that has not been reported to date. Furthermore, a rank-matrix is proposed with carefully decided weights for performance parameters as a systematic approach to selecting the WF at given operating conditions. Finally, this study researches the usage of geographic information systems in thermodynamic analyses, machine learning algorithms to aid in selecting optimal WF for specified cycle operation conditions.

2. SYSTEM DESCRIPTION

Working fluids considered for this study were selected based on their critical conditions (critical temperature and critical pressure), environmental impact (global warming and ozone depletion potential), and operating cycle pressures and temperature [18][19]. Initially, fourteen WFs were chosen for analyses, and then they are screened to three WFs. The screening of an initially large number of WFs was also carried out in a study by Das *et al.* [20], with the procedure discussed in detail in Appendix D. Table 1 lists the three WFs whose thermodynamic performances were compared in this work. These WFs finally selected all having a low level of toxicity as listed by the American Society of Heating, Refrigerating, and Air-Conditioning Engineers (ASHRAE) safety group designation [18]. The capital letter in the ASHRAE safety group designates a toxicity class, while the numeral denotes flammability [18]. According to ASHRAE Standard 34, class 'A' denotes refrigerants of lower toxicity, and class 'B' denotes higher toxicity. The numeral 1 denotes refrigerants having no flame propagation (NFP), and numerals 2L and 2 denote refrigerants of low flammability, with 2L having flammability values between 1 and 2, and the numeral 3 representing the group of the refrigerant having high flammability [18].

Table 1 also includes global warming potential (GWP) and ozone depletion potential (ODP) values used to interpret the impact that a particular WF has on the environment. According to the Kigali Amendment of the Montreal Protocol [21], low GWP and low ODP WFs should be employed to reduce the impact on the environment.

GWP is the measure of energy the emissions of 1 ton of a gas will absorb over a given time, relative to the emissions of 1 ton of CO_2 [22]. According to the United States Environmental Protection Agency (EPA), ODP is the ratio of the impact of a chemical on ozone compared to the impact of a similar mass of CFC-11 on ozone. The impact of CFC-11 on ozone is defined to be 1 [23].

Table 1. Applicable properties and characteristics of the working fluid in this study [20]

Fluid Name	T_c (K)	P_c (kPa)	GWP	ODP	Flammability	ASHRAE Safety Group
Dimethyl Ether	400	5367	1	<0	High	A3
R-1234yf	368	3382	<1	0	Low	A2L
Diethyl Ether	467	3644	4±2	<0	High	A3

In this study, the three primary WFs, shown in Table 1, are all organic fluids, and they are referred to as pure WFs. Zeotropic mixtures (ZM) are also studied herein by combining the WFs from Table 1 and carbon dioxide (CO_2). Furthermore, the performances of the chosen WFs are compared to conventional fluids used in power generation and low-temperature operation. The properties and characteristics of these auxiliary WFs used in the analyses are given in Table 2.

Table 2. Applicable properties and characteristics of the auxiliary working fluid in this study [20][24][25]

Fluid Name	T_c (K)	P_c (kPa)	GWP	ODP	Flammability	ASHRAE Safety Group
Carbon Dioxide	304	7377	1	0	NFP	A1
R-12 (CFC)	385	4136	10200	1.0	NFP	A1
R-22 (HCFC)	369	4990	1760	0.055	NFP	A1
Water	647	22064	0.2±0.2	0	NFP	A1

The ORC is a modified Rankine cycle operating on organic fluids instead of a natural fluid (water) in a cycle that includes four major components of a pump, an evaporator, a turbine, and a condenser, as shown in Figure 1. The ORC working with pure WFs can be operated above or below the critical point of the fluid. Figure 2 shows the temperature entropy (T-s) diagram of an ORC where the WF exiting the condenser in the saturated-liquid phase is pumped to the evaporator pressure (P_2) and then heated in the heat exchanger by a low-grade heat-source to the turbine inlet temperature (T_3). Depending on the mode of cycle operation (subcritical or supercritical), evaporator pressure is above or below the critical pressure of the WF. The high pressure and high-temperature WF are then expanded in the turbine to the condenser pressure (P_4), generating power before entering the condenser, and the cycle continues. Equally spaced heat-source inlet temperatures (T_5), 400 K through 500 K, and two heat-sink temperatures (T_7) of 277 K and 300 K are considered in this study. The dead state is assumed to be at the ambient temperature and pressure of the average annual temperature of the corresponding US city and 101.325 kPa, respectively, in all cases. The uncertainty in the

measured values of temperature (T_0, T_5, T_7) and pressure (P_0, P_5, P_7) are assumed to be ±1 K and 0.1% of the measured value, respectively, as shown in Table 3. Unless stated otherwise, the temperature differences between the cycle and the heat-source in the evaporator, $\delta T_1 = T_5 - T_3$, and between the cycle and the heat-sink in the condenser $\delta T_2 = T_1 - T_7$, in Figure 1, is 10 K. The cycle analyses are carried out for a fixed turbine output power of 250 kW.

3. THERMODYNAMIC ANALYSIS

Several Python scripts were developed to compute the energy and exergy analyses of the system using thermophysical properties obtained from reference fluid thermodynamic and transport properties (REFPROP), a National Institute of Standards and Technology (NIST) database [26] for a given operating condition. A wrapper class was utilized to obtain various values of thermophysical properties from REFPROP while utilizing the python environment.

The cycle considered in this work (Figure 1) is assumed to be operating at a steady-state condition and having no pressure loss in the system. The T-s diagrams for sub-critical and super-critical operations of the cycle were shown in Figure 2 and Figure 3, respectively. The isentropic efficiencies for the pump and the turbine are assumed to be 85% and 80%, respectively. The heat-source is assumed to be hot air entering the evaporator at point 5 in a counter-flow arrangement with a constant flow rate of 20 kg/s, while the heat-sink is assumed to be water entering the condenser at point 7, also following a counter-flow heat exchange with a constant flow rate of 10 kg/s.

Uncertainty analysis was conducted for all cycle parameters on the assumed uncertainties of the cycle inlet parameters, as shown in Table 3 [20]. The propagated uncertainty was then computed, as indicated throughout this work, except for ZMs due to the complex nature of computation. ZMs are formed using the innate capability of REFPROP to blend multiple WF in either molar or mass basis. For this study, the ZMs are based on a molar basis.

Table 3. Uncertainty assumptions of the considered variables

Parameters	Uncertainty Assumption
Temperature differences between WF and the heat-source in an evaporator, δT_1	1 K
Temperature differences between WF and the cold sink in a condenser, δT_2	1 K
Isentropic Efficiency of Pump	0.2 %
Isentropic Efficiency of Turbine	0.2 %
Dead State Temperature, T_0	1 K
Dead State Pressure, P_0	0.1 %
Heat-source Temperature, T_5	1 K
Heat-source Pressure, P_5	0.1 %
Heat-sink Temperature, T_7	1 K
Heat-sink Pressure, P_7	0.1 %
The flow rate of hot air in the evaporator, m_5	0.2 kg/s
The flow rate of cold water in the condenser, m_7	0.1 kg/s

3.1. Energy Analyses

The employment of the energy analyses is to analyze the performance of ORCs as shown in Figure 2 and Figure 3 based on the first law of thermodynamics for the given operating conditions. The thermodynamic relations used in the analyses are from standard thermodynamics textbooks [27][28]. The thermophysical properties of ZMs are computed based on similar relations as the pure WFs. However, due to the complex nature of ZM, this study does not include calculations related to forming the ZMs. These computations are made using REFPROP, which yields a similar result as PR van der Waals co-volume equation for mixing and Peng–Robinson Equation-of-State for calculating physical properties [29].

3.1.1. First Law Efficiency

The first law efficiency (η) is defined as the ratio of effective work done by the cycle to the heat input to the cycle from the heat-source.

$$\eta = \left(\frac{W_{net}}{Q_{in}}\right) \times 100 \quad (1)$$

where, W_{net} represents the effective work output of the cycle and is given by,

$$W_{net} = W_{turb} - W_{pump} \quad (2)$$

where, W_{turb} represents the work done by the turbine, W_{pump} is the work done on the pump, and Q_{in} is the heat input to the cycle from the hot source.

$$W_{pump} = m_f(h_2 - h_1) \quad (3)$$

$$Q_{in} = m_{hs}(h_5 - h_6) \quad (4)$$

where *h* is the enthalpy and *m* is the mass flow rate, while subscripts *f* and *hs*, indicating the WF and hot source flow, respectively. The evaporator used in this study is a shell-and-tube type heat exchanger and modeled like Das et al. [20]

3.1.2. Second Law Efficiency

The second law efficiency (η_2) of a cycle is defined as the ratio of effective work done by the cycle to the exergy input from the heat-source and is given by,

$$\eta_2 = \left(\frac{W_{net}}{EX_I}\right) \times 100 \quad (5)$$

The exergy input from a heat-source is the maximum possible heat energy that could be transferred from the heat-source to the cycle for given temperature reservoirs.

$$EX_I = Q_{in}\left(1 - \frac{T_0}{T_3}\right) \quad (6)$$

3.1.3. Volume Power Coefficient

Like the refrigeration cycle, where Volume Refrigeration Capacity (VRC) measures system sizing, Das et al. [18] defined a new parameter to describe the system sizing characteristics in an ORC. Volume power coefficient (*VPC*) is defined as the ratio of turbine output power to the volume flow rate at the outlet of the turbine. The higher value of *VPC* is indicative of the better performance of the cycle in terms of sizing, as the greater value of *VPC* suggests a lower volume flow of WF producing the same turbine output.

$$VPC = \frac{W_{turb}}{m_f v_3} \tag{7}$$

The mass flow rate of the WF in the cycle is given by,

$$m_f = \frac{W_{turb}}{h_3 - h_4} \tag{8}$$

3.2. Exergy Analyses

Exergy is defined as the maximum work obtained from an amount of available energy in a process under an ideal condition, while Exergy-destruction is a measure of resource degradation and represents lost work potential [30][31]. The specific exergies at a state point, i in the system is found by,

$$ex_i = \left((h_i - h_0) - T_0(s_i - s_0)\right) \tag{9}$$

where h_i and s_i represent the state enthalpy and entropy, respectively, T is temperature, and subscripts *i* and *o* represent the specific state point and ambient condition. The exergy-destruction in the evaporator is calculated as follow,

$$XD_{evap} = Q_{in}\left[1 - \frac{T_0}{T_3}\right] + m_f(ex_2 - ex_3) \tag{10}$$

Dimensionless exergy-destruction in the evaporator is defined as the ratio of exergy-destruction in the evaporator to the exergy input to the cycle.

$$\lambda = \frac{XD_{evap}}{Q_{in}\left[1-\frac{T_0}{T_3}\right]} \tag{11}$$

The dimensionless exergy-destruction in the evaporator and the second law efficiency seem the same, but they differ significantly. The dimensionless exergy-destruction in the evaporator is an exergy parameter corresponding to a component, while the second law efficiency showcases the exergy-efficiency of the entire cycle. Higher values of second law efficiency are desirable. In contrast, dimensionless exergy-destruction in the evaporator should be minimized for better operation.

3.3. Thermodynamic Databases

The results showcased by Das et al. [20] are computed using the Engineering Equation Solver (EES) thermodynamic database, which is based on the Fundamental Equation-of-State [32]. However, for this work, REFPROP is used in conjunction with an in-house python program to obtain the results. REFPROP uses the NIST database for property calculations. It is imperative to check both databases before analyzing the findings in the present study. The operating cycle in Das et al. [20] of heat-source inlet temperatures of T_5 = 400, 450, and 500 and heat-sink temperatures of T_7 = 300 K is used for this purpose, and calculated performance for different WFs using both databases are compared. Figure 4 shows the comparison of the first law efficiency (η) obtained using EES (solid lines) and REFPROP (dashed line) databases and for different reduced pressure (θ). The η trends obtained from both databases follow a similar trend; however, the values do not match exactly, primarily due to different Equation-of-State usage by the different

databases. It appears that EES-based calculations are a maximum of 1.5% lower than those of REFPROP.

With the trends being similar for both databases and low difference in parameter values, the validity of the results obtained by the EES database in the publication made by Das et al. [20] also holds for the current study's findings using the REFPROP database.

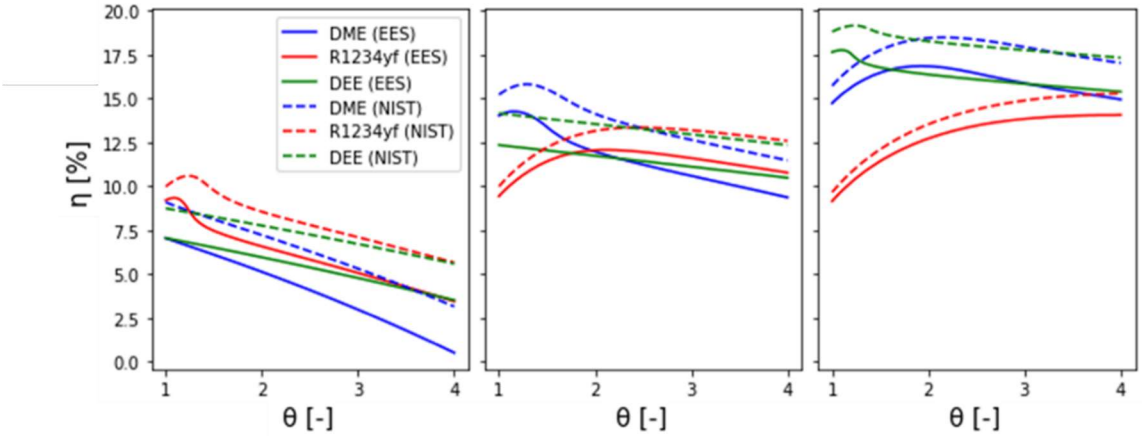

Figure 4. Variation of first law efficiency of different thermodynamic databases with θ at heat-sink temperature, T_7 = 300 K, and different heat-source temperatures

3.4. Selection of Heat-sink Temperature

The average annual temperature of fifty cities in the U.S. is obtained from Table 7 and Table 8. The bivariate linear fit of latitude of these U.S. cities, using average annual temperatures, is shown in Figure 5 and is obtained by JMP. A high negative correlation of 0.91±0.01 between average annual temperature and latitude suggests a robust linear relationship and justifies the use of this latitude-temperature distribution to select condenser temperature for this study. Figure 6 shows the latitude distribution of the U.S. cities with the count as the ordinate and average annual temperature as the abscissa. The distribution shows most cities having an average annual temperature in the class range of

285 K through 290 K. For this study, two condenser temperatures are considered for analysis; these values closely correspond to the quartiles of the distribution. The boxplot in Figure 6 states a positively skewed distribution with a higher mean value than the median. The lower and higher condenser temperature is thereby assumed to be 277 K and 300 K, respectively.

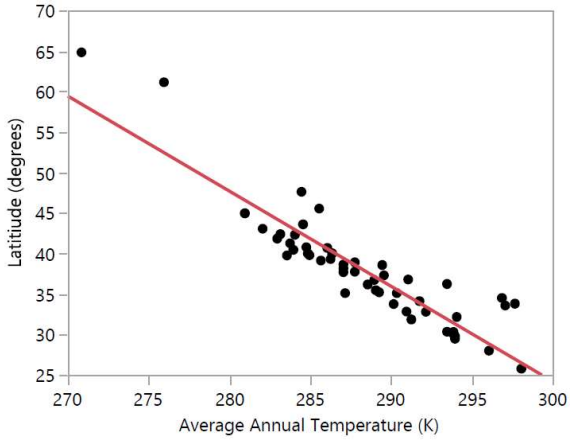

Figure 5. The bivariate fit of latitude (in degrees of U.S. cities) by the average annual temperature of U.S. cities

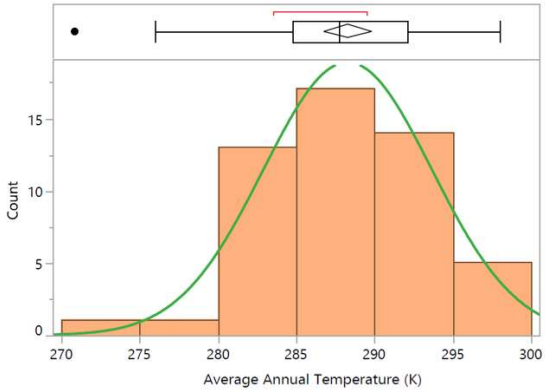

Figure 6. Histogram with boxplot for distribution of latitude (in degrees of U.S. cities) and average annual temperature of U.S. cities

4. CYCLE OPERATION WITH PURE WORKING FLUIDS

Cycle analysis was carried out for all the combinations of heat-source inlet temperatures (T_5) and heat-sink temperatures (T_7), along with the variations of reduced pressures (θ). The reduced pressure is the ratio of evaporator pressure (P_2) to the critical pressure of the WF (P_c). Analyzing the cycle performance in terms of reduced pressure is critical owing to the heat transfer challenges of operating in a pseudocritical region of the WF. The reduced pressure is varied from half through three in order to study both subcritical and supercritical cycle operations. Three heat-source inlet temperatures selected for this study are T_5 = 400 K, 450 K, and 500 K. The two chosen heat-sink temperatures (T_7) of 277 K and 300 K are at a difference of two standard deviations from the mean ambient temperature, across fifty cities of the U.S. Shown in Figure 7 through Figure 13 for several parameter and analyzed below in this chapter are variations of first law efficiency (η), dimensionless exergy-destruction of the evaporator (λ), second law efficiency (η_2), and volume power coefficient (VPC) for dimethyl ether (DME), R1234yf, and diethyl ether (DEE).

4.1. First Law Efficiency

Figure 7 shows the first law efficiency (η) of the ORC as a function of reduced pressure (θ) for the WFs at different combinations of heat-source inlet temperatures of T_5 and heat-sink temperature of T_7. The vertical orange line in Figure 7 represents the critical pressure of the working fluids ($\theta = 1$). Hence, the area on the left of the line represents the cycle operation at the subcritical state, while the supercritical cycle operation is the region

to the right of the vertical orange line. The plots were constructed from 50 data points using the NIST database for computation.

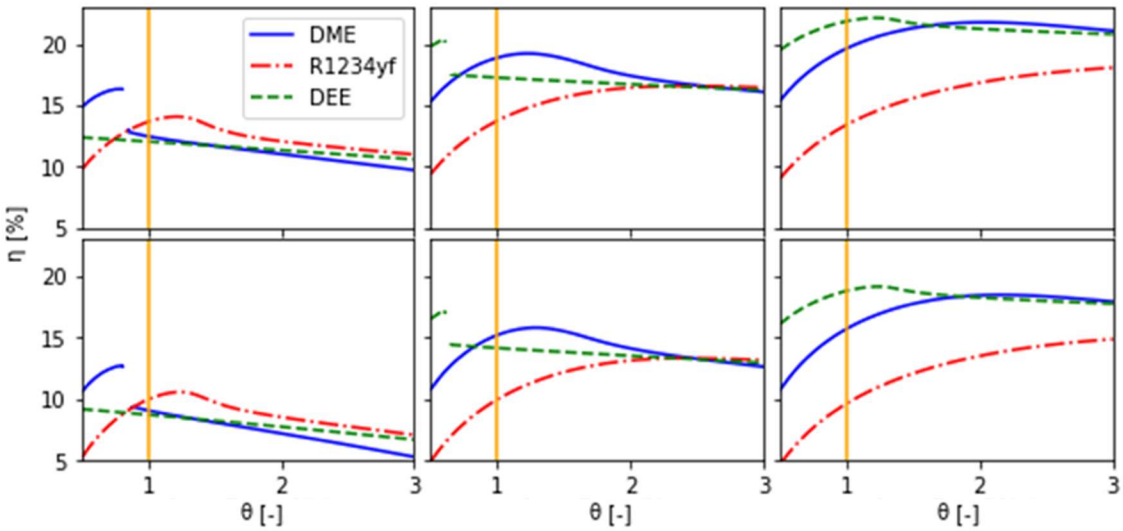

Figure 7. Variation of first law efficiency with θ for heat-source temperature left to the right column, T_5 = 400 K, 450 K, 500 K, and heat-sink temperature, top, and bottom rows, T_7 = 277 K, 300 K, respectively

The subcritical cycle has a reduced pressure (θ) value of less than one. At heat-source inlet temperatures (T_5) of less than and equal to 450 K, peak first law efficiency values are found in the subcritical region. At heat-source inlet temperature of 400 K, DME has a peak efficiency of 16.3%and 12.7% at T_7 of 277 K and 300 K, respectively. While, at heat-source inlet temperature of 450 K, DEE has a peak efficiency of 20.6% and 17.2% at T_7 of 277 K and 300 K, respectively in the subcritical region. At a heat-source temperature of 500 K, peak cycle efficiencies are observed in the supercritical region of operation. For subcritical operation, DME and DEE are better performing fluids than R1234yf.

The first row of Figure 7 shows the variation of first law efficiency (η) for the WFs at different heat-source inlet temperatures (T_5) at a heat-sink temperature of 277 K. Figure 8 shows the reduced pressure in subcritical range, θ = 0.5 to 1, for a detailed study. At heat-source inlet temperature of 400 K, DME shows a better cycle performance of 16.3% at 4302 kPa compared to other WFs.

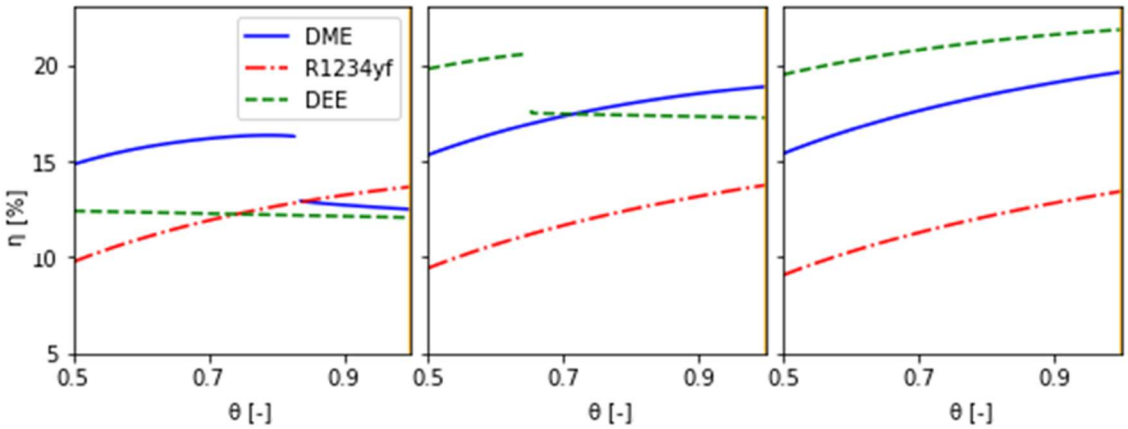

Figure 8. Variation of first law efficiency with θ for heat-source temperature left to the right column, T_5 = 400 K, 450 K, 500 K and heat-sink temperature, T_7 = 277 K

At reduced pressure of 0.835, there is a 20.8% sudden decrease in the first law efficiency of DME. On further investigation, the sudden decrease in the value of first law efficiency can be attributed to the effective work done by the ORC. Effective work done by the ORC is referred to as net work done by the cycle, which is the difference between turbine output power and pump power consumption. The trends in Figure 9 can better explain this phenomenon. For example, the turbine output power is constant for the setup; hence, the drop in the efficiency is due to an increase of pump work at θ = 0.835. The increase of pump work culminates in a lower amount of effective work, thereby reducing

the first law efficiency. A further investigation carried out on this sudden change in values is discussed in detail in Appendix C.

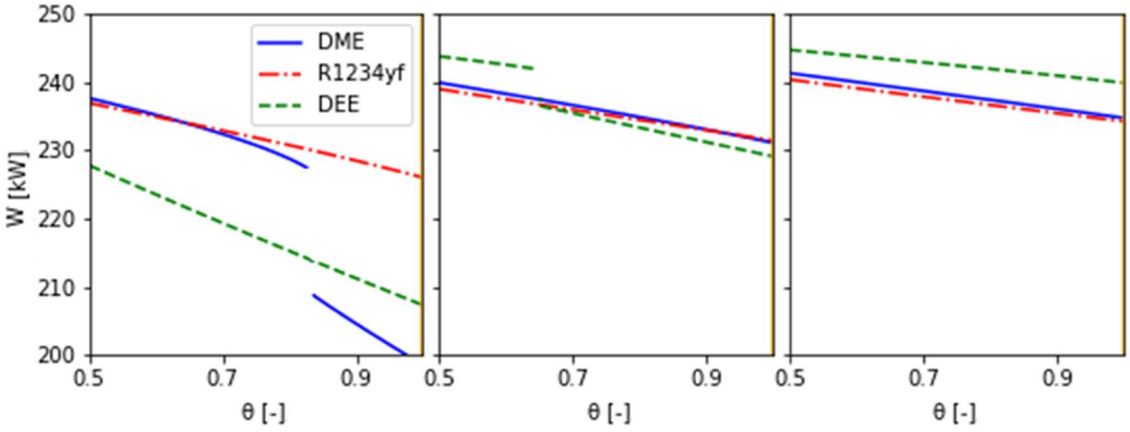

Figure 9. Variation of effective work done with θ for heat-source temperature left to the right column, T_5 = 400 K, 450 K, 500 K and heat-sink temperature, T_7 = 277 K

At a heat-source inlet temperature of 450 K, DEE shows a peak efficiency value of 20.6% at 2343 kPa, after which at a reduced pressure of 0.72, DME starts exhibiting better first law efficiency trends as shown in Figure 8. R1234yf also shows similar pattern at a heat-source inlet temperature of 400 K as made by DME at 450 K.

At a heat-source inlet temperature of 500 K, DEE is the best WF with a first law efficiency value above 20%. However, DEE does not exhibit its peak efficiency in the subcritical region, and the first law efficiency values increase monotonically with reduced pressure.

The second row of Figure 7 shows first law efficiency (η) for the WFs at different heat-source inlet temperatures (T_5) and a heat-sink temperature of 300 K. Contrary to Figure 8, in Figure 10 the reduced pressure is revised to be in subcritical range, θ = 0.5 to 1, for a detailed study. At a heat-source inlet temperature of 400 K, DME shows a better

cycle performance of 12.7% at 4357 kPa compared to other WFs. At a reduced pressure of 0.84, there is a 25.1% decrease in the first law efficiency of DME compared to the value for a reduced pressure of 0.83 values due to approaching the pseudocritical region.

At a heat-source inlet temperature of 450 K, DEE shows a peak efficiency value of 17.4% at 2343 kPa, after which at a reduced pressure of 0.84, DME starts exhibiting better first law efficiency trends. At a heat-source inlet temperature of 500 K, DEE is the best WF. However, DEE does not exhibit its peak efficiency in the subcritical region, and the first law efficiency values increase monotonically with reduced pressure similar to a lower condenser temperature of 277 K.

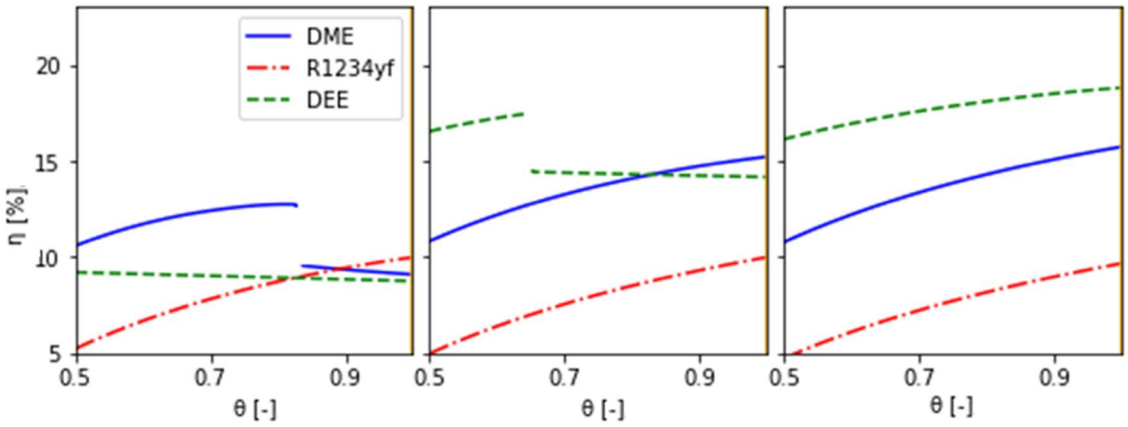

Figure 10. Variation of first law efficiency with θ for heat-source temperature left to the right column, T_5 = 400 K, 450 K, 500 K and heat-sink temperature, T_7 = 300 K

The supercritical cycle has a reduced pressure (θ) value greater than one. Figure 7 shows that at an inlet temperature of more than 450 K, the peak first law efficiency value is exhibited in the supercritical region. DEE has a peak efficiency of 22.1% (θ = 1.20) and 19.2% (θ = 1.24) at T_7 of 277K and 300 K, respectively, for heat-source inlet temperature of 500 K. For supercritical operations, DEE is the best-performing fluid.

For heat-source inlet temperature of 400 K, R1234yf performs better in the supercritical region than the other WFs. At condenser temperatures of 277 K and 300 K, a peak first law efficiency of 14.0% at 4072 kPa and 10.6% at 4211 kPa are recorded, respectively. However, DME achieves a maximum first law efficiency at this 400 K heat-source inlet temperature in the subcritical region.

Similarly, at a heat-source inlet temperature of 450 K, DME has a better performance in the supercritical region compared to the other WFs. At condenser temperatures of 277 K and 300 K, a peak first law efficiency of 19.2%at 6644 kPa and 15.8% at 6862 kPa are recorded, respectively. However, DEE achieved a maximum first law efficiency at this 450 K heat-source inlet temperature in the subcritical region.

The first law efficiency (η) trends for heat-sink temperature (T_7) of 277 K and 300 K at both subcritical and supercritical modes of operation are similar. However, the first law efficiency trends at a heat-sink temperature of 277 K has a higher value, owing to the higher Carnot first law efficiency compared to a heat-sink temperature of 300 K for the given heat-source temperature.

4.2. Dimensionless Exergy-destruction of Evaporator

Figure 11 shows the dimensionless exergy-destruction of the evaporator (λ) for the WFs as a function of reduced pressure at different combinations of heat-source inlet temperatures, T_5 = 400 K, 450 K, 500 K, and heat-sink temperatures T_7 = 277 K, 300 K. Dimensionless exergy-destruction of evaporator (λ) trends are formed by the variation of input heat energy and the difference in exergy at the inlet and outlet of the evaporator [20]. A lower λ value is more desirable, as the lower value signifies the higher exergy-efficiency

of the cycle. The subplot area left of the vertical orange line (θ = 1) in Figure 11 is the subcritical cycle operation. At all heat-source inlet temperatures (T_5), peak dimensionless exergy-destruction of evaporator (λ) values is found in the subcritical region.

At a heat-source inlet temperature of 400 K, DME has the best λ = 0.30at T_7 = 277 K, and λ = 0.20at T_7 = 300 K. At a heat-source inlet temperature of 450 K, DEE has the best λ value of 0.32 at T_7 = 277 K, and 0.24 at T_7 of 300 K. DEE's superiority in performance at T_5 = 450 K is until a reduced pressure θ = 0.65 at T_7 = 277 K and 0.74 at T_7 = 300 K is reached, after which the DME showcases better λ characteristics for the remaining reduced pressure range.

At heat-source temperature of 500 K, DEE again exhibits the best λ values of 0.36 at T_7 of 277 K and 0.30 at T_7 of 300 K for both subcritical and supercritical operations in comparison with all WFs. Cycle operation at a higher condenser temperature of 300 K has a lower exergy-destruction compared to operation at a lower condenser temperature of 277 K. The sudden increase of λ values at heat-source inlet temperatures of 400 K and 450 K is analogous to the already discussed phenomenon of sudden decreases of first law efficiency (η) values at the same reduced pressure (θ) values and supported by the findings in Figure 9.

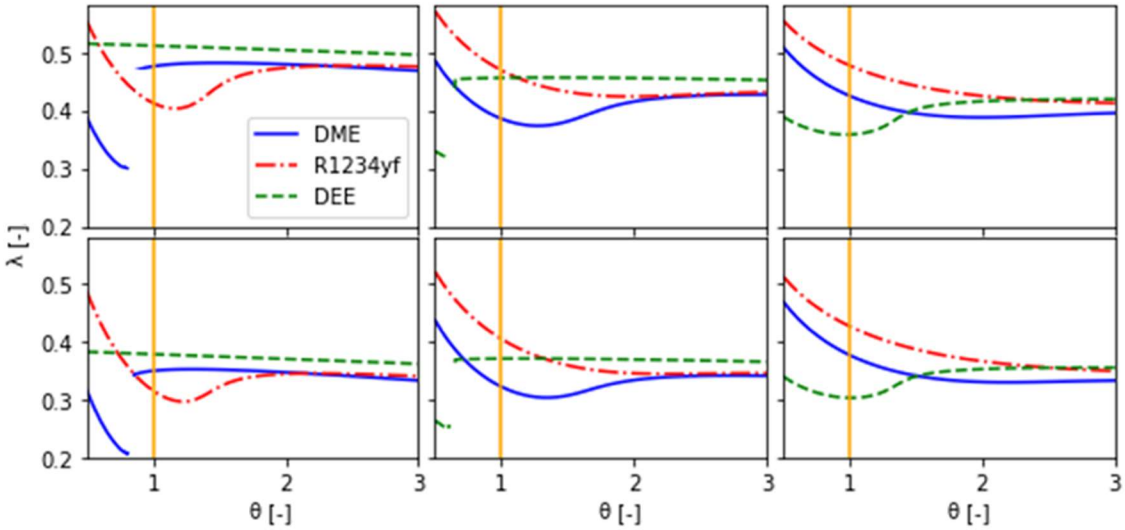

Figure 11. Variation of dimensionless exergy-destruction of the evaporator with θ for heat-source temperature left to the right column, T_5 = 400 K, 450 K, 500 K, and heat-sink temperature, top, and bottom rows, T_7 = 277 K, 300 K, respectively

The supercritical cycle has a reduced pressure (θ) value greater than one. Dimensionless exergy-destruction of the evaporator (λ) at all heat-source inlet temperatures shows better values in the subcritical region. At a heat-source inlet temperature of 400 K, R1234yf shows a better performance than DME and DEE, while at higher heat-source inlet temperatures of 450 K and 500 K, the DME and DEE, respectively, showcases superior performances amongst the WFs.

For the entire range of reduced pressure, a subcritical operation is found to have lower dimensionless exergy-destruction of evaporator (λ) values, with DME and DEE being the better performing WF.

4.3. Second Law Efficiency

Figure 12 shows the second law efficiency (η_2) of the cycle for the WFs as a function of reduced pressure (θ) at different combinations of heat-source inlet

temperatures, T_5 = 400 K, 450 K, 500 K, and heat-sink temperature T_7 = 277 K, 300 K. This plot closely resembles the trends observed in Figure 7, as second law efficiency is effective work done to the exergy input of the cycle, which is similar to first law efficiency being effective work done to the heat input to the cycle.

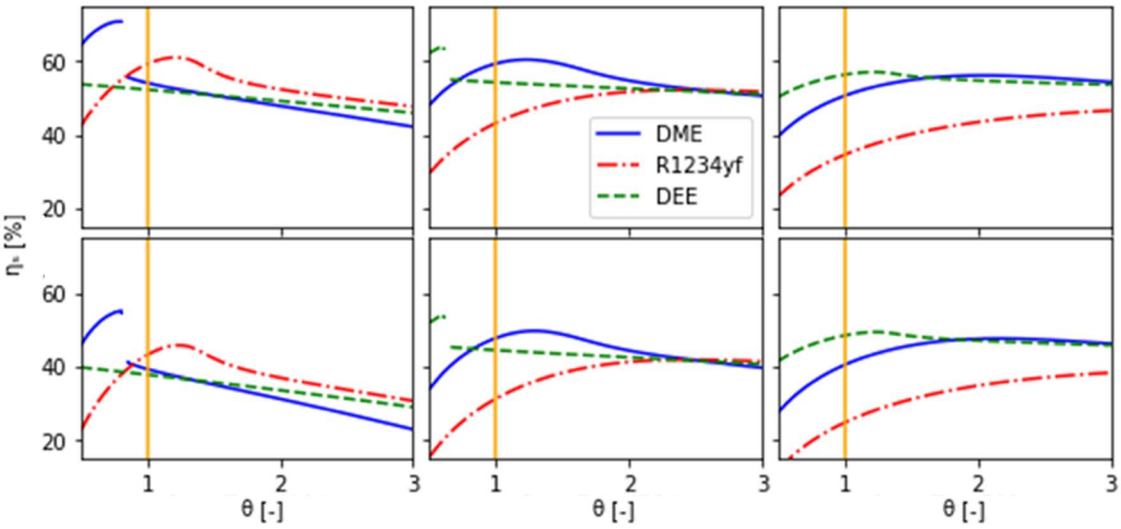

Figure 12. Variation of second law efficiency with θ for heat-source temperature left to the right column, T_5 = 400 K, 450 K, 500 K, and heat-sink temperature, top, and bottom rows, T_7 = 277 K, 300 K, respectively

The subcritical cycle has a reduced pressure (θ) value of less than one. At heat-source inlet temperatures (T_5) of less than or equal to 450 K, peak second law efficiency values are found in the subcritical region. At heat-source inlet temperatures of 400 K and 450 K, DME has peak second law efficiency of 70.8% at T_7 of 277 K and 55.2% at T_7 of 300 K, while DEE has a value of 64.6% at T_7 of 277 K, 54.8% at T_7 of 300 K, in the subcritical region.

At a heat-source temperature of 500 K, peak cycle efficiencies are observed in the supercritical region of operation for DEE followed by DME. For subcritical operations, DME and DEE are better performing fluids than R1234yf.

The supercritical cycle has a reduced pressure (θ) value greater than one. At heat-source inlet temperatures of 400 K and 450 K, the second law efficiency value peaks in the subcritical region. Specifically, at a heat-source inlet temperature of 500 K, DEE has peak second law efficiency of 57.0% at T_7 of 277 K and 49.4% at T_7 of 300 K. For supercritical operations, DEE is the best-performing fluid at 500 K.

For a heat-source inlet temperature of 400 K, R1234yf performs better in the supercritical region than the other WFs. At condenser temperatures of 277 K and 300 K, a peak second law efficiency of 61.0% at 4072 kPa and 45.8% at 4211 kPa are recorded, respectively. However, DME achieves a maximum first law efficiency at this heat-source inlet temperature in the subcritical region.

Similarly, at a heat-source inlet temperature of 450 K, DME has a better performance in the supercritical region compared to the other WFs. At condenser temperatures of 277 K and 300 K, a peak first law efficiency of 60.4% at 6644 kPa and 49.7% at 6862 kPa are recorded, respectively. However, DEE achieved a maximum first law efficiency at this heat-source inlet temperature in the subcritical region.

The second law efficiency (η_2) for heat-sink temperature (T_7) of 277 K and 300 K at both subcritical and supercritical mode of operation show similar trends to the first law efficiency (η) plots, which can be attributed to η_2 being the function of η and Carnot first law efficiency.

4.4. Volume Power Coefficient

The volume power coefficient (*VPC*) is represented by a turbine power ratio to the WF's volume flow rate at the turbine's inlet [20]. The higher value of *VPC* is indicative of the better performance of the cycle in terms of sizing, as the greater value of *VPC* suggests a lower volume flow of WF producing the same turbine output. Figure 13 shows the volume power coefficient (*VPC*) for the WFs as a function of reduced pressure at different combinations of heat-source inlet temperatures, T_5 = 400 K, 450 K, 500 K, and heat-sink temperatures T_7 = 277 K, 300 K. As evident from Figure 13, *VPC* shares a positive correlation with reduced pressure, and the best performance can be found in the supercritical range for every heat-source inlet temperature.

The subcritical cycle has a reduced pressure (θ) value of less than one. At all heat-source inlet temperatures (T_5), peak *VPC* values in the subcritical region are for DEE. However, *VPC* increases monotonically with reduced pressure (θ), and the peak values for a combination of heat-source inlet temperature and condenser temperature can be found in the supercritical range of operation. Similar to previous parameters (η, λ, η_2), there is a sudden increase in values at heat-source inlet temperatures of 400 K and 450 K for DME and DEE, respectively. These changes are attributed to the explanations provided in Appendix C.

The supercritical cycle has a reduced pressure (θ) value greater than one. At a heat-source inlet temperature of 400 K, peak *VPC* values are exhibited in the supercritical region by both DME and DEE. However, at heat-source inlet temperatures of 450 K and 500 K, DEE has peak *VPC* values. For supercritical operation and an entire range of

operation, DEE has the best system sizing characteristics with better values of *VPC* compared to other WFs.

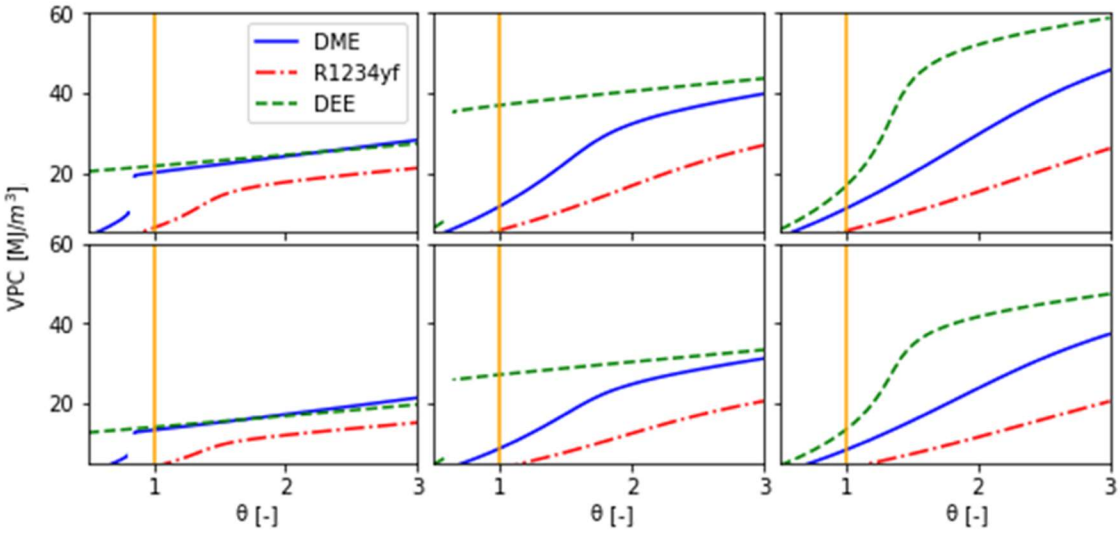

Figure 13. Variation of *VPC* with θ for heat-source temperature left to the right column, T_5 = 400 K, 450 K, 500 K, and heat-sink temperature, top, and bottom rows, T_7 = 277 K, 300 K, respectively

5. CYCLE OPERATION WITH ZEOTROPIC MIXTURES

A zeotropic mixture (ZM) for a working fluid is a mixture of two components that have different boiling points [33]. Individual WFs comprising a ZM do not evaporate or condense at the same temperature as one substance, indicating the mixture has a temperature glide [34]. The phase change occurs in a ZM over a temperature range of about 4˚ C to 7˚ C rather than at a single saturation temperature [34].

According to ASHRAE, the three pure WFs (DME, R1234yf, and DEE) are highly flammable [18] so that these pure WFs, analyzed in the previous section, are mixed with CO_2 to form ZMs that are less flammable than the component WF. The ZMs are formed on a molar basis, and the REFPROP wrapper class function is used in python script to form the blends and to obtain their thermodynamic properties. According to Pursell et al. [35][36], 60% CO_2 on a molar basis is required to induce complete inertness to the mixture of HC and CO_2. The resultant three ZMs (DME and CO_2, R1234yf and CO_2, DEE and CO_2), whose performance is discussed in the section below, have 60% CO_2 blended with their respective WFs on a molar basis.

Cycle analysis is carried out for all the combinations of heat-source inlet temperatures (T_5) and heat-sink temperatures (T_7) at a variety of reduced pressures (θ), which is defined as the ratio of evaporator pressure (P_2) to the critical pressure of the ZM (P_c). The critical pressure of the ZM varies with the fractional molar composition of the components in the mixture. For this study, the critical pressure of a ZM corresponds to the critical pressure of a ZM of pure WFs (DME, R1234yf, and DEE) and CO_2 in the molar

ratio of 40:60. Analyzing the cycle performance in terms of reduced pressure is critical owing to the heat transfer challenges of operating in the pseudocritical region of the WF. The reduced pressure is varied from half through three to cater to both subcritical and supercritical operations of the cycle. An analysis using Figure 14 through Figure 17 was conducted on four performance factors, namely first law efficiency (η), dimensionless exergy-destruction of the evaporator (λ), second law efficiency (η_2), and volume power coefficient (VPC) for the ZMs of dimethyl ether and carbon dioxide (DME: CO_2), R1234yf, and carbon dioxide (R1234yf: CO_2), and diethyl ether and carbon dioxide (DEE: CO_2). The results of these analyses are presented below.

5.1. First Law Efficiency

Figure 14 shows the first law efficiency (η) for the ZMs as a function of reduced pressure (θ) of the mixtures at different combinations of heat-source inlet temperatures, T_5 = 400 K, 450 K, and 500 K, and a heat-sink temperature T_7 = 277 K and 300 K. The molar composition of all the mixtures is made up of 60% CO_2 on a molar basis, while the rest of 40% constitutes the pure HC.

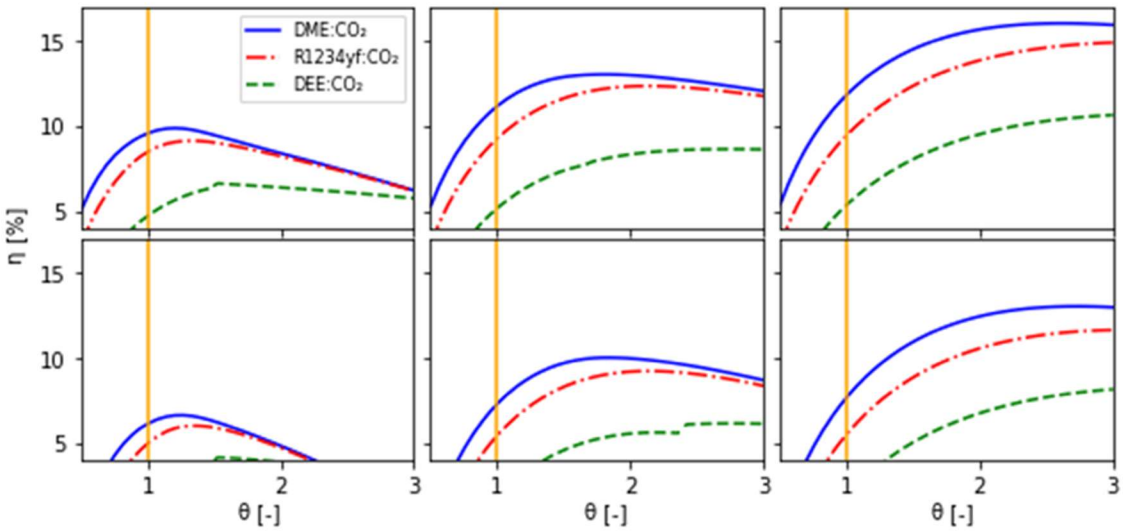

Figure 14. Variation of first law efficiency with θ of zeotropic mixtures for heat-source temperature left to the right column, T_5 = 400 K, 450 K, 500 K, and heat-sink temperature, top, and bottom rows, T_7 = 277 K, 300 K, respectively

The subcritical cycle operation has a reduced pressure (θ) value of less than one. The most efficient cycle performance lies in the supercritical region for all heat-source inlet temperature and heat-sink temperature combinations. The subcritical region is characterized by a steady increase of first law efficiency with reduced pressure. For ZMs, in terms of first law efficiency, a subcritical mode of operation is not desirable due to inefficient cycle operation. The higher efficiency in the supercritical mode of operation can be attributed to a better temperature match between the heat-source and the ZM outside the realm of the dome, as shown in Figure 3.

The supercritical cycle has a reduced pressure (θ) value greater than one and lies right of the orange vertical line, as shown in Figure 14. At all heat-source inlet temperatures, the ZM of DME and CO_2 at the molar ratio (40:60) in the supercritical region exhibit a peak first law efficiency value. The trend exhibited by most of the

mixtures in the supercritical region is a steady increase in first law efficiency. The trend continuation from the subcritical region is a peak value, followed by a monotonic decrease in efficiency values for the rest of the range of the reduced pressure. The efficiency values at a heat-sink temperature of 277 K have better results than a higher heat-sink temperature of 300 K, as shown in Figure 14, indicating the similarity with the Carnot efficiency.

At a heat-source inlet temperature of 400 K, 450 K and 500 K, peak first law efficiency values of 9.9% at θ of 1.21 (10258 kPa), 13.0% at θ of 1.78 (15169 kPa), and 16.0% at θ of 2.62 (22263 kPa) are recorded for ZM of DME and CO_2 for a heat-sink temperature of 277 K. The ZM of DME and CO_2 at the molar ratio (40:60) considered here is the best operating ZM in comparison to the rest of the mixtures.

5.2. Dimensionless Exergy-destruction of Evaporator

Figure 15 shows the dimensionless exergy-destruction of the evaporator (λ) for the ZMs as a function of reduced pressure (θ) of the mixtures at different combinations of heat-source inlet temperatures, T_5 = 400 K, 450 K, 500 K, and heat-sink temperature T_7 = 277 K, 300 K. Dimensionless exergy-destruction of evaporator (λ) trends are formed by the variation of input heat energy and the difference in exergy at the inlet and outlet of the evaporator [20].

The dimensionless exergy-destruction of the evaporator (λ) is higher for lower heat-sink temperature. Lower values of λ signify better cycle performance, and clearly, operation in the supercritical region and at a higher heat-sink temperature of 300 K (second row in Figure 15) is more favorable.

At a heat-source inlet temperature of 400 K, 450 K, and 500 K, the ZM of R1234yf and CO_2 has the best λ characteristics of 0.28, 0.31, and 0.33 at $\theta = 3$. However, for most of the operating pressures, the ZM of DME and CO_2 has better performance than other blends.

In the supercritical region of operation at a higher heat-source inlet temperature of 450 K and higher, λ characteristics are comparable for the ZM of DME and CO_2 and ZM of R1234yf and CO_2. For a heat-source inlet temperature of 400 K, the ZM of DME and CO_2 is recommended; however, for 450 K and 500 K, both ZMs of DME and R1234yf with CO_2 at the molar ratio (40:60) are an appropriate choice.

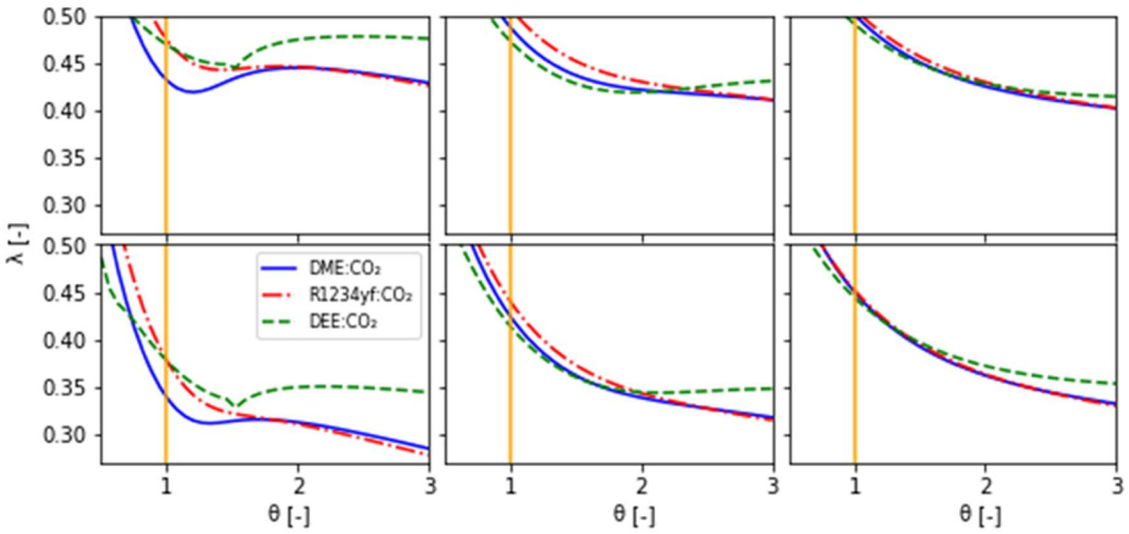

Figure 15. Variation of dimensionless exergy-destruction of the evaporator (λ) with θ of zeotropic mixtures for heat-source temperature, left to the right column, T_5 = 400 K, 450 K, 500 K, and heat-sink temperature, top, and bottom rows, T_7 = 277 K, 300 K, respectively

5.3. Second Law Efficiency

Figure 16 shows the second law efficiency (η_2) for the ZMs as a function of reduced pressure (θ) for different combinations of heat-source inlet temperatures, T_5 = 400 K, 450 K, and 500 K, and heat-sink temperatures T_7 = 277 K and 300 K. This plot closely resembles the trends observed in Figure 14, with the reason being second law efficiency is effective work done to the exergy input of the cycle, which is similar to first law efficiency being effective work done to the heat input to the cycle.

Similar to the trends of first law efficiency as shown in Figure 14, second law efficiency peak values are recorded for the supercritical range of operation at a lower heat-sink temperature of 277 K. The ZM of DME and CO_2 at the molar ratio (40:60) considered here has the best performance amongst all the mixtures. At a heat-source temperature of 400 K, 450 K and 500 K; peak second law efficiency values of 42.8% at θ of 1.21 (10258 kPa), 41.0% at θ of 1.78 (15169 kPa), and 41.4% at θ of 2.62 (22263 kPa), respectively are recorded.

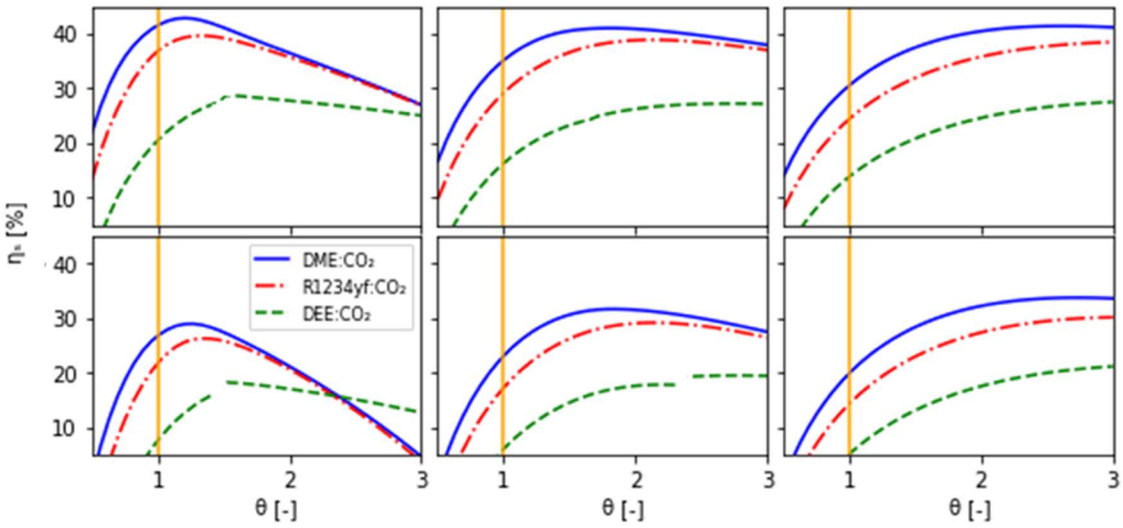

Figure 16. Variation of second law efficiency with θ of zeotropic mixtures for heat-source temperature left to the right column, T_5 = 400 K, 450 K, 500 K, and heat-sink temperature, top, and bottom rows, T_7 = 277 K, 300 K, respectively

5.4. Volume Power Coefficient

Like the refrigeration cycle, where VRC measures system sizing, a new parameter has been defined by Das et al. [20] to describe the system sizing characteristics in an ORC. Figure 17 shows the *VPC* for the ZMs as a function of reduced pressure at different combinations of heat-source inlet temperatures, T_5 = 400 K, 450 K, and 500 K, and heat-sink temperature T_7 = 277 K and 300 K. *VPC* trends are formed by turbine power ratio to the WF volume flow rate at the turbine inlet [20]. A higher value of *VPC* is indicative of the better performance of the cycle in terms of sizing, as a greater value of *VPC* suggests a lower volume flow of WF producing the same turbine output.

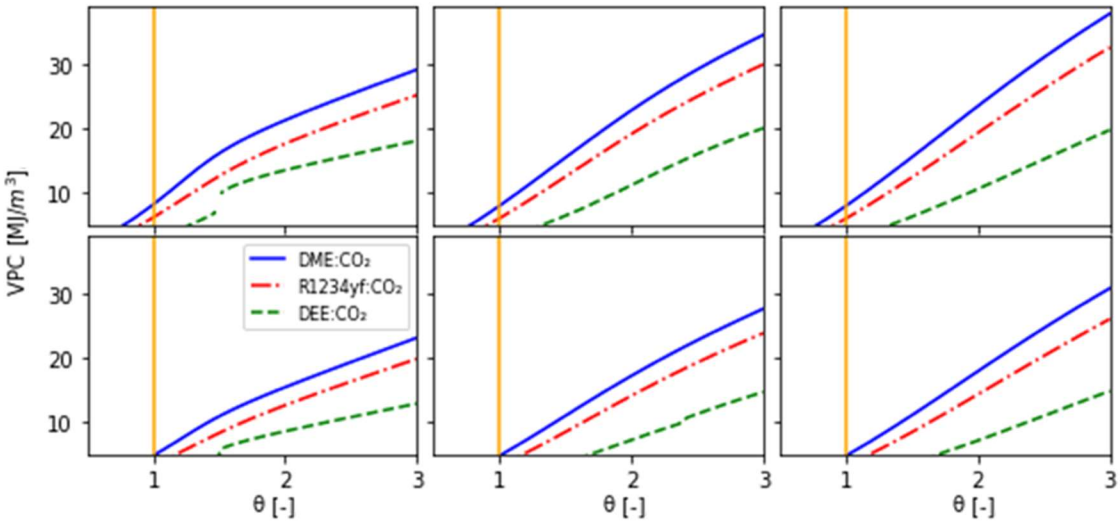

Figure 17. Variation of VPC with θ of zeotropic mixtures for heat-source temperature left to the right column, T_5 = 400 K, 450 K, 500 K, and heat-sink temperature, top, and bottom rows, T_7 = 277 K, 300 K, respectively

As observed in Figure 17, *VPC* shares a positive correlation with reduced pressure for the ZMs, and the best performance can be found in the supercritical range at every heat-source inlet temperature for the ZM of DME and CO_2. The value of *VPC* is higher at a lower heat-sink temperature of 277 K, which is similar to first law efficiency trends.

Considering all the performance parameters, the ZM of DME and CO_2 at the molar ratio (40:60) considered here is the best ZM for a wide range of operating temperatures and pressures.

6. COMPARATIVE FLUID ANALYSIS

The results in the previous chapters discuss the performance of either pure WFs or ZMs of these WFs with CO_2 on a 40:60 molar basis. Until now, in this study, for the same operating conditions, the cycle performances of pure WFs were not compared to ZMs.

The most commonly used WF for power generation is water, and it was ignored in this analyses because of the emphasis herein on low-grade waste heat. Freons also with their widespread usage in the refrigeration cycle, were not part of a performance comparison. Before selecting WF/ ZM for a given set of operating conditions, it is important to compare performances to standard WFs, like water and freons.

6.1. Pure working fluid to zeotropic mixture

Figure 18 shows the trends in first law efficiency (η) for both the ZM of DME and CO_2 at the molar ratio (40:60) and the pure WFs (DME, R1234yf, and DEE) as a function of reduced pressure (θ) of the mixtures at different combinations of heat-source inlet temperatures, T_5 = 400 K, 450 K, 500 K, and heat-sink temperature T_7 = 277 K, 300 K.

For all combinations of heat-source temperatures, T_5 and heat-sink temperatures, T_7, the ZM of DME and CO_2 with a molar ratio (40:60) has a performance that is lower than its pure WF counterparts.

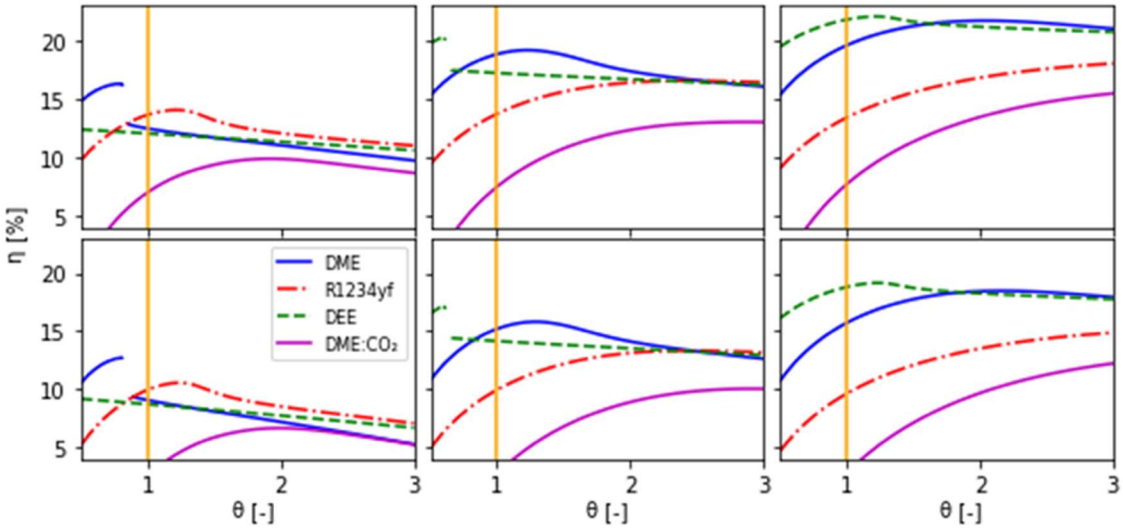

Figure 18. Variation of first law efficiency with θ of zeotropic mixtures and pure working fluids for heat-source temperature left to the right column, T_5 = 400 K, 450 K, 500 K, and heat-sink temperature, top, and bottom rows, T_7 = 277 K, 300 K, respectively

6.2. Water and Freons

Figure 19 shows the trends in first law efficiency (η) for both the ZM of DME and CO_2 at the molar ratio (40:60), and common WFs, namely freons and water, as a function of reduced pressure (θ) of the mixtures at different combinations of heat-source inlet temperatures, T_5 = 400 K, 450 K, 500 K, and heat-sink temperature T_7 = 277 K, 300 K.

Freons, broadly classified as CFCs and HCFCs, are the most used refrigerants in the twentieth century. These refrigerants have better first law efficiency trends at all combinations of heat-source temperature, T_5 and heat-sink temperature, T_7 than the ZM of DME and CO_2; however, they have high values of GWP and ODP, as shown in Table 2. According to the Kigali Amendment to the Montreal Protocol [21], CFCs and HCFCs are

under a mandatory phase out, even though the first law efficiency of these CFCs and HCFCs are comparable to the pure WFs.

Water is the most commonly used WFs for power generation used in thermal power plants and nuclear power plants. On the first look of Figure 19, it appears that water has a comparable performance to the ZM; however, the critical pressure of water (22064 kPa) when accounted for would suggest a more robust system design compared to other organic WFs or ZMs. The performance of water being comparable to ZM of DME and CO_2 in all the combinations of heat-source temperature, T_5, and heat-sink temperature, T_7, would suggest an inferior performance compared to the rest of WFs.

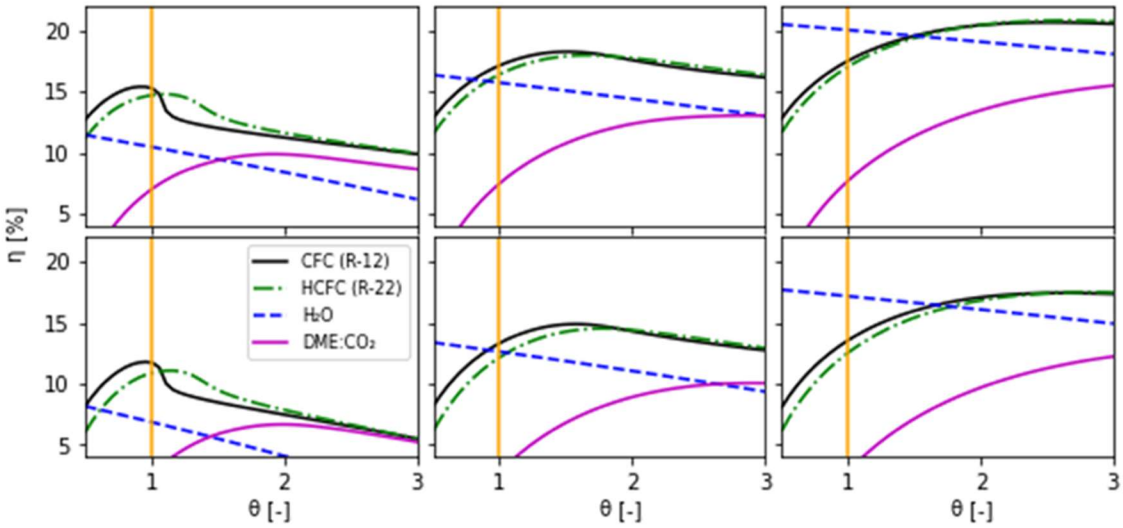

Figure 19. Variation of first law efficiency with θ of zeotropic mixtures, freons, and water for heat-source temperature, left to the right column, T_5 = 400 K, 450 K, 500 K and heat-sink temperature, top, and bottom rows, T_7 = 277 K, 300 K, respectively

7. CLIMATE PROFILING

Detailed analyses on the performance of organic WFs and ZMs have been carried out in the previous chapters. However, the aim of the study is climate profiling and selection of the best fit WFs at a given system condition of heat-source and heat-sink temperatures for various cities of U.S. In the previous chapters, with their focus on specific combination of heat-source temperatures and heat-sink temperatures, it was possible to hint at the optimal WF for these conditions. However, for fifty cities with different heat-sink temperatures, it would be tedious to predict the optimal WF manually, and a need for a systematic method needs to be devised.

A rank-matrix is proposed for the selection of WFs for a given condition. All the parameters analyzed before are considered with appropriately assigned weightings. First law efficiency (η) and second law efficiency (η_2) have a combined weightage of 0.55, as an efficient operation is pivotal to the cycle's operation. The dimensionless exergy-destruction of the evaporator (λ) is assigned a weightage of 0.35, considering the importance of efficacy on cycle operations, which obtains input heat energy from an external source. Lastly, a weightage of 0.10 is attributed to the volume power coefficient (VPC) parameter as it represents sizing and economic characteristics of the cycle.

The average annual temperature obtained from Table 4 and Table 5 is considered to be the cycle's heat-sink temperature for each city. The rank-matrix is employed to estimate the optimal WF at all three heat-source temperatures. The WF with the highest

aggregate score (higher on the rank list) is chosen with its operating state (value of reduced pressure) for the stated temperature conditions.

Table 4 through Table 6 are tabulations of the values of three performance parameters, namely first law efficiency, volume power coefficient, and dimensionless exergy-destruction of evaporator, for those optimal WFs selected at specific heat-sink, heat-source temperatures, and operating pressures. For example, DME is the WF chosen for 400 K and 450 K, while DEE is for a heat-source temperature, T_5 of 500 K.

As shown in Table 4, DME is the optimal WF for all the cities, meaning it is best suited for the temperature difference between the ambient conditions in these cities and the heat-source temperature of 400 K. The reduced pressure ranges from 0.77 through 0.83, suggesting a subcritical mode of operation for the heat-source temperature of 400 K, across all locations. As shown in Figure 8, the first law efficiency (η) for DME exceeds that of DEE and R1234yf by a minimum of 3% in the reduced pressure range. The higher weightage assigned to cycle efficiencies (first and second), ensures the selection of DME as the optimal WF for these working conditions. The first law efficiency (η) has a mean value of 14.6% with a standard deviation of 0.84%, and the dimensionless exergy-destruction of the evaporator (λ) has a mean value of 0.35 with a standard deviation of 0.10. The heat-sink temperature, which is the average annual temperature of the cities, has a mean of 288.3 K with a standard deviation of 5.33 K.

Table 4. City-wise variation of optimal operating condition and values of performance parameters for DME at heat-source temperature, T_5 of 400 K

City	η (%)	*VPC* (kW/m^3)	λ (-)	*Operating Pressure (kPa)*
Albuquerque	14.7	8318	0.33	4286
Anchorage	16.5	9737	0.12	4286
Atlanta	14.3	7954	0.38	4286
Austin	13.7	7514	0.45	4286
Baltimore	14.9	8429	0.31	4286
Boise	15.1	8639	0.28	4286
Boston	15.2	8701	0.27	4286
Charlotte	14.4	8062	0.37	4286
Chicago	15.4	8839	0.25	4286
Columbus	15.1	8602	0.28	4286
Dallas	14.0	7715	0.42	4286
Denver	15.3	8764	0.26	4286
Detroit	15.4	8814	0.25	4286
El Paso	14.1	7822	0.40	4286
Fairbanks	17.3	9562	0.02	4129
Fresno	14.1	7846	0.40	4286
Houston	13.7	7502	0.46	4286
Indianapolis	15.1	8589	0.28	4286
Jacksonville	13.8	7561	0.45	4286
Kansas City	15.0	8503	0.30	4286
Las Vegas	13.8	7561	0.45	4286
Lake Havasu City	13.2	7921	0.51	4442
Los Angeles	14.0	7762	0.41	4286
Louisville	14.8	8330	0.32	4286
Memphis	14.2	7930	0.39	4286
Miami	13.0	7770	0.54	4442
Milwaukee	15.5	8953	0.23	4286
Minneapolis	15.7	9092	0.21	4286
Nashville	14.5	8147	0.35	4286
New Orleans	13.7	7514	0.45	4286
New York City	14.9	8453	0.31	4286
Oklahoma City	14.4	8087	0.36	4286
Omaha	15.3	8739	0.26	4286
Palm Springs	13.1	7820	0.53	4442

City	η (%)	*VPC* (kW/m^3)	λ (-)	*Operating Pressure (kPa)*
Philadelphia	14.9	8416	0.31	4286
Phoenix	13.2	7896	0.52	4442
Pittsburgh	15.2	8714	0.27	4286
Portland (OR)	15.0	8515	0.30	4286
Sacramento	14.4	8038	0.37	4286
Salt Lake City	15.1	8614	0.28	4286
San Antonio	13.7	7502	0.46	4286
San Diego	14.1	7858	0.40	4286
San Francisco	14.6	8245	0.34	4286
San Jose	14.4	8026	0.37	4286
Seattle	15.2	8652	0.27	4286
St. Louis	14.8	8330	0.32	4286
Tampa	13.3	8023	0.50	4442
Tucson	13.7	7490	0.46	4286
Virginia Beach	14.5	8099	0.36	4286
Washington D.C.	14.6	8245	0.34	4286
Wichita	14.8	8330	0.32	4286

In Table 5, again similar to the heat-source temperature of 400 K, DME is the optimal WF for all cities, meaning it is best suited to the temperature difference between the ambient conditions in these cities and the heat-source temperature of 450 K. The reduced pressure ranges from 1.21 through 1.3, hinting at a supercritical mode of operation for the heat-source temperature of 450 K, across all locations. As shown in Figure 7, the first law efficiency (η) for DME in the supercritical region at the specified reduced pressure range is higher than DEE and R1234yf. Consequently, the second law efficiency for DME is higher in value. Also, the dimensionless exergy-destruction of the evaporator (λ), as shown in Figure 11 for DME, is lower than DEE and R1234yf. However, DEE has

better *VPC* characteristics, such that a minor weightage of 0.10 ends in the selection of DME as the optimal WF for the working conditions.

Table 5. City-wise variation of optimal operating condition and values of performance parameters for DME at heat-source temperature, T_5 of 450 K

City	η (%)	*VPC* (kW/m^3)	λ (-)	*Operating Pressure (kPa)*
Albuquerque	17.7	15281	0.56	6787
Anchorage	19.4	16666	0.42	6631
Atlanta	17.3	14755	0.60	6787
Austin	16.7	14673	0.63	6943
Baltimore	17.8	15440	0.54	6787
Boise	18.1	15743	0.52	6787
Boston	18.2	15833	0.51	6787
Charlotte	17.4	14912	0.59	6787
Chicago	18.3	16031	0.50	6787
Columbus	18.0	15690	0.52	6787
Dallas	17.0	14409	0.63	6787
Denver	18.2	15923	0.51	6787
Detroit	18.3	15995	0.50	6787
El Paso	17.1	14565	0.62	6787
Fairbanks	20.1	16931	0.37	6474
Fresno	17.1	14599	0.61	6787
Houston	16.7	14656	0.63	6943
Indianapolis	18.0	15672	0.53	6787
Jacksonville	16.8	14744	0.63	6943
Kansas City	17.9	15547	0.54	6787
Las Vegas	16.8	14744	0.63	6943
Lake Havasu City	16.3	14149	0.67	6943
Los Angeles	17.0	14478	0.62	6787
Louisville	17.7	15299	0.56	6787
Memphis	17.2	14721	0.60	6787
Miami	16.1	13941	0.69	6943
Milwaukee	18.5	15580	0.51	6631
Minneapolis	18.6	15774	0.49	6631
Nashville	17.5	15035	0.58	6787
New Orleans	16.7	14673	0.63	6943

City	η (%)	*VPC* (kW/m^3)	λ (-)	*Operating Pressure (kPa)*
New York City	17.9	15476	0.54	6787
Oklahoma City	17.4	14947	0.58	6787
Omaha	18.2	15887	0.51	6787
Palm Springs	16.2	14010	0.69	6943
Philadelphia	17.8	15423	0.55	6787
Phoenix	16.2	14114	0.68	6943
Pittsburgh	18.2	15851	0.51	6787
Portland (OR)	17.9	15565	0.53	6787
Sacramento	17.4	14877	0.59	6787
Salt Lake City	18.1	15708	0.52	6787
San Antonio	16.7	14656	0.63	6943
San Diego	17.1	14617	0.61	6787
San Francisco	17.6	15175	0.57	6787
San Jose	17.4	14860	0.59	6787
Seattle	18.1	15761	0.52	6787
St. Louis	17.7	15299	0.56	6787
Tampa	16.4	14288	0.66	6943
Tucson	16.7	14638	0.63	6943
Virginia Beach	17.4	14965	0.58	6787
Washington D.C.	17.6	15175	0.57	6787
Wichita	17.7	15299	0.56	6787

At a heat-source temperature of 500 K, DEE is the optimal WF for all the cities, as shown in Table 6, meaning it is best suited to the temperature difference between the ambient conditions in these cities. The reduced pressure ranges from 1.39 through 1.48, which indicates a supercritical mode of operation for the heat-source temperature of 500 K across all locations. As shown in Figure 7 and Figure 11, the first law efficiency (η) and dimensionless exergy-destruction of the evaporator (λ) for DME and DEE in this specified reduced pressure range are comparable. However, DEE has superior *VPC* characteristics, as shown in Figure 13, which gives it an edge over DME as the optimal WF.

Table 6. City-wise variation of optimal operating condition and values of performance parameters for DEE at heat-source temperature, T_5 of 500 K

City	η (%)	*VPC* (kW/m^3)	λ (-)	*Operating Pressure (kPa)*
Albuquerque	20.5	35628	0.77	5168
Anchorage	22.0	39572	0.67	5168
Atlanta	20.1	34615	0.80	5168
Austin	19.7	33392	0.83	5168
Baltimore	20.6	35935	0.76	5168
Boise	20.8	38018	0.73	5275
Boston	20.8	38199	0.73	5275
Charlotte	20.2	34917	0.79	5168
Chicago	20.9	39895	0.71	5381
Columbus	20.7	37910	0.74	5275
Dallas	19.9	33951	0.81	5168
Denver	20.9	38380	0.72	5275
Detroit	20.9	39819	0.71	5381
El Paso	20.0	34249	0.80	5168
Fairbanks	22.7	39471	0.64	5061
Fresno	20.0	34315	0.80	5168
Houston	19.6	33359	0.83	5168
Indianapolis	20.7	37873	0.74	5275
Jacksonville	19.7	33523	0.82	5168
Kansas City	20.6	37622	0.74	5275
Las Vegas	19.7	33523	0.82	5168
Lake Havasu City	19.2	34857	0.83	5381
Los Angeles	19.9	34083	0.81	5168
Louisville	20.5	35662	0.77	5168
Memphis	20.1	34549	0.80	5168
Miami	19.0	34442	0.84	5381
Milwaukee	21.0	40236	0.70	5381
Minneapolis	21.2	40655	0.69	5381
Nashville	20.3	35153	0.78	5168
New Orleans	19.7	33392	0.83	5168
New York City	20.6	36003	0.76	5168
Oklahoma City	20.3	34984	0.79	5168
Omaha	20.9	38307	0.73	5275
Palm Springs	19.1	34580	0.83	5381

City	η (%)	*VPC* (kW/m^3)	λ (-)	*Operating Pressure (kPa)*
Philadelphia	20.6	35901	0.76	5168
Phoenix	19.1	34788	0.83	5381
Pittsburgh	20.9	38235	0.73	5275
Portland (OR)	20.6	37658	0.74	5275
Sacramento	20.2	34850	0.79	5168
Salt Lake City	20.7	37946	0.73	5275
San Antonio	19.6	33359	0.83	5168
San Diego	20.0	34349	0.80	5168
San Francisco	20.4	35424	0.77	5168
San Jose	20.2	34816	0.79	5168
Seattle	20.8	38054	0.73	5275
St. Louis	20.5	35662	0.77	5168
Tampa	19.3	35136	0.82	5381
Tucson	19.6	33327	0.83	5168
Virginia Beach	20.3	35018	0.78	5168
Washington D.C.	20.4	35424	0.77	5168
Wichita	20.5	35662	0.77	5168

At a heat-source temperature of 400 K, the subcritical mode of operation with DME as the WF gives the optimal performance, while at higher heat-source temperatures, a supercritical mode of operation is more optimum. DME and DEE are the choice of WFs for heat-source temperatures of 450 K and 500 K, respectively. The weights assigned to various parameter groups have been made by the author based on the importance of parameters; however, these are not absolute, and modifications to the weights can be made to obtain better distribution compared to that made in this study. Additionally, the average annual temperature is based on data for a year, while a decade's worth of monthly temperature data would yield more accurate results. The reduced pressure varies from half through three with thirty distinct points at regular intervals, leading to a coarser data mesh.

Due to its computationally intensive nature, more points could not be studied, and future work is required in this regard. Supervised machine learning algorithms can also be used to replace the rank-matrix method for selecting WFs. This study is unique as it attempts to organize the systematic prediction of the WF and its operation conditions for given temperatures.

8. CONCLUSIONS

In this study, three pure WFs and three ZMs comprised of the pure WFs with CO_2 at a 40:60 molar basis were considered as potential WFs for an ORC. The performance evaluations were carried out on a low-grade waste heat-source with temperatures varying from 400 K to 500 K for a given heat-sink temperature associated with a city in the U.S. at a constant turbine output of 250 kW. Energy and exergy analyses were used to determine parameters to be in a rank-matrix method for selecting the optimal WF. A Python script and REFPROP, which is a NIST database, were used to carry out the necessary computations. The significance of the current work is the selection of WFs with low environmental impacts and superior performance based on climate profiling of temperatures, along with optimal cycle operating conditions to optimize the utilization of available waste heat-sources and ambient conditions. The limitation of the current study include:

- The working fluid selection is based on the specific operating conditions (i.e., temperatures, pressures, and work output) assumed in this study. Additional studies would have to be performed for operations under different conditions.
- The working fluids selected for different heat-source temperatures are highly flammable HCs. The current study considers a single blend of zeotropic mixtures, while better performing, yet chemically inert, zeotropic mixture should be the subject of a future study.

- A rank-matrix is used to select the optimal working fluid and operating conditions. Advanced techniques with a higher volume of data can be used with machine learning techniques to provide a more precise prediction.

The main conclusions of this study are summarized below:

- For a heat-source inlet temperature of 400 K, the subcritical mode of operation with DME as the working fluid is preferred. SORC is the choice of cycle operations at 450 K and 500 K heat-source inlet temperatures with DME and DEE as the working fluids, respectively.
- At various heat-sink temperatures, corresponding to the average annual temperature of U.S. cities, the optimal operating pressure of the cycle for heat-source inlet temperatures of 400 K, 450 K, and 500 K is estimated to be 4298±52 kPa, 6803±93 kPa for dimethyl ether, and 5226±85 kPa for diethyl ether, respectively.

REFERENCES

[1] Organic Rankine cycle. (2020, September 24). Retrieved January 19, 2021, from https://en.wikipedia.org/wiki/Organic_Rankine_cycle#:~:text=The%20low%2Dtemperature%20heat%20is,Bronicki%20and%20Harry%20Zvi%20Tabor.

[2] Johnson, Ilona, Choate, William T., & Davidson, Amber. Waste Heat Recovery. Technology and Opportunities in U.S. Industry. United States. https://doi.org/10.2172/1218716

[3] Sarkar, J. (2015). Review and future trends of supercritical CO2 Rankine cycle for low-grade heat conversion. Renewable and Sustainable Energy Reviews, 48, 434-451. doi:10.1016/j.rser.2015.04.039

[4] Javanshir, A., & Sarunac, N. (2017). Thermodynamic analysis of a simple Organic Rankine Cycle. Energy, 118, 85-96. doi:10.1016/j.energy.2016.12.019

[5] Desai, N. B., & Bandyopadhyay, S. (2009). Process integration of organic Rankine cycle. Energy, 34(10), 1674-1686. doi:10.1016/j.energy.2009.04.037

[6] Karellas, S., & Schuster, A. (2008). Supercritical Fluid Parameters in Organic Rankine Cycle Applications. International Journal of Thermodynamics, 11(3), 101–108.

[7] Mikielewicz, J., & Mikielewicz, D. (2009). Comparative study of selected fluids for use in supercritical Organic Rankine Cycles. Archives of Thermodynamics, 30(2), 3–14.

[8] Gao, H., Liu, C., He, C., Xu, X., Wu, S., & Li, Y. (2012). Performance Analysis and Working Fluid Selection of a Supercritical Organic Rankine Cycle for Low Grade Waste Heat Recovery. Energies, 5(9), 3233-3247. doi:10.3390/en5093233

[9] Vidhi, R., Kuravi, S., Goswami, D. Y., Stefanakos, E., & Sabau, A. S. (2013). Organic Fluids in a Supercritical Rankine Cycle for Low Temperature Power Generation. Journal of Energy Resources Technology, 135(4). doi:10.1115/1.4023513

[10] Vetter, C., Wiemer, H., & Kuhn, D. (2013). Comparison of sub- and supercritical Organic Rankine Cycles for power generation from low-temperature/low-enthalpy geothermal wells, considering specific net power output and efficiency. Applied Thermal Engineering, 51(1-2), 871-879. doi:10.1016/j.applthermaleng.2012.10.042

[11] Wang, X., Levy, E. K., Pan, C., Romero, C. E., Banerjee, A., Rubio-Maya, C., Pan, L. (2019). Working fluid selection for organic Rankine cycle power generation using hot produced supercritical CO2 from a geothermal reservoir. Applied Thermal Engineering, 149, 1287-1304. https://doi.org/10.1016/j.applthermaleng.2018.12.112

[12] Mudasar, R., Aziz, F., Kim, M. (2017). Thermodynamic analysis of organic Rankine cycle used for flue gases from biogas combustion. Energy Conversion and Management, 153, (627-640). https://doi.org/10.1016/j.enconman.2017.10.034.

[13] Quoilin, S., Broek, M.V.D., Declaye, S., Dewallef, P., Lemort, V. (2013). Techno-economic survey of Organic Rankine Cycle (ORC) systems. Renewable and

Sustainable Energy Reviews, 22, 168-186. https://doi-org.srv-proxy2.library.tamu.edu/10.1016/j.rser.2013.01.028
[14] Ozdil, N. F. T., Segmen, M. R., Tantekin, A. (2015). Thermodynamic analysis of an Organic Rankine Cycle (ORC) based on industrial data. Applied Thermal Engineering, 91, (43-52). https://doi.org/10.1016/j.applthermaleng.2015.07.079.
[15] Deethayat, T., Kiatsiriroat, T., & Thawonngamyingsakul, C. (2015). Performance analysis of an organic Rankine cycle with internal heat exchanger having zeotropic working fluid. Case Studies in Thermal Engineering, 6, 155-161. doi:10.1016/j.csite.2015.09.003
[16] Wang, W., Deng, S., Zhao, D., Zhao, L., Lin, S., Chen, M. (2020). Application of machine learning into organic Rankine cycle for prediction and optimization of thermal and exergy efficiency. Energy Conversion and Management, 210. https://doi.org/10.1016/j.enconman.2020.112700.
[17] Rodrigues, A., Gonçalves, A. B., Casquilho, M., & Gomes, A. A. (2020). A GIS-based evaluation of the potential of Woody Short Rotation Coppice (SRC) in Portugal aiming at co-firing and decentralized co-generation. Biomass and Bioenergy, 137, 105554. doi:10.1016/j.biombioe.2020.105554
[18] Addenda to Standard 34-2016. (n.d.). Retrieved June 27, 2020, from https://www.ashrae.org/technical-resources/standards-and-guidelines/standards-addenda/addenda-to-standard-34-2016
[19] Yelishala, S. C., Kannaiyan, K., Wang, Z., Metghalchi, H., Levendis, Y. A., & Sadr, R. (2020). Thermodynamic study On blends of hydrocarbons and carbon dioxide AS Zeotropic Refrigerants. Journal of Energy Resources Technology, 142(8). doi:10.1115/1.4045930
[20] Das, D., Kazim, M., Sadr, R., & Pate, M. (2021). Optimal hydrocarbon based working fluid selection for a Simple SUPERCRITICAL Organic Rankine cycle. Energy Conversion and Management, 243, 114424. doi:10.1016/j.enconman.2021.114424
[21] (n.d.). Retrieved September 21, 2021, from https://www.epa.gov/ozone-layer-protection/recent-international-developments-under-montreal-protocol
[22] (n.d.). Retrieved September 22, 2021, from https://www.epa.gov/ghgemissions/understanding-global-warming-potentials
[23] (n.d.). Retrieved September 22, 2021, from https://www.epa.gov/ozone-layer-protection/ozone-depleting-substances
[24] Intergovernmental Panel on Climate Change. (2014). Anthropogenic and Natural Radiative Forcing. In Climate Change 2013 – The Physical Science Basis: Working Group I Contribution to the Fifth Assessment Report of the Intergovernmental Panel on Climate Change (pp. 659–740). chapter, Cambridge: Cambridge University Press. http://doi.org/10.1017/CBO9781107415324.018
[25] Forster, P., Ramaswamy, V., Artaxo, P., Berntsen, T., Betts, R., Fahey, D.W., Haywood, J., Lean, J., Lowe, D.C., Myhre, G., Nganga, J., Prinn, R., Raga, G., Schulz, M., & Van Dorland, R. Miller, H.L. (Ed.). (2007). Changes in Atmospheric Constituents and in Radiative Forcing Chapter 2. United Kingdom: Cambridge University Press.

[26] Lemmon, E. , Huber, M. and McLinden, M. (2013), NIST Standard Reference Database 23: Reference Fluid Thermodynamic and Transport Properties-REFPROP, Version 9.1, Natl Std. Ref. Data Series (NIST NSRDS), National Institute of Standards and Technology, Gaithersburg, MD, [online], https://tsapps.nist.gov/publication/get_pdf.cfm?pub_id=912382 (Accessed September 3, 2021)
[27] Klein, S. A., & Nellis, G. (2012). Thermodynamics. Cambridge University Press.
[28] Nag, P. K. (1993). Engineering thermodynamics. New Delhi.
[29] Wu, Y., Zhang, H., Zhang, Q., Qiu, J., & Rui, S. (2017). The study of thermodynamic properties of zeotropic mixtures of r600a/r23/r14. Advances in Mechanical Engineering, 9(3), 168781401769121. doi:10.1177/1687814017691214
[30] Dinçer, I., & Rosen, M. (2021). Exergy: Energy, environment and sustainable development. Amsterdam, Netherlands: Elsevier.
[31] Whiting, K., Carmona, L. G., & Sousa, T. (2017). A review of the use of exergy to evaluate the sustainability of fossil fuels and non-fuel mineral depletion. Renewable and Sustainable Energy Reviews, 76, 202-211. doi:10.1016/j.rser.2017.03.059
[32] Engineering Equation Solver for Microsoft Windows Operating Systems. Retrieved from https://engineering.purdue.edu/ME300/EES-manual.pdf [accessed on 01.13.2021].
[33] Gaspar, D. P., & Da, S. P. (2015). Handbook of research on advances and applications in refrigeration systems and technologies. Engineering Science Reference, an imprint of IGI Global.
[34] Mohanraj, M., Muraleedharan, C., & Jayaraj, S. (2010). A review on recent developments in new refrigerant mixtures for vapour compression-based refrigeration, air-conditioning and heat pump units. International Journal of Energy Research, 35(8), 647-669. doi:10.1002/er.1736
[35] Gant, S., Pursell, M., Lea, C., Fletcher, J., Rattigan, W., Thyer, A., & Connolly, S. (2011). Flammability of hydrocarbon and carbon dioxide mixtures. Process Safety and Environmental Protection, 89(6), 472-481. doi:10.1016/j.psep.2011.06.017
[36] Pursell, M. R. (2011). Flammability of hydrocarbon/CO2mixtures: Part 1. Ignition and explosion characteristics (Institution of Chemical Engineers Symposium Series, pp. 440-449). Institution of Chemical Engineers. Retrieved September 13, 2021, from https://www-engineeringvillage-com.srv-proxy2.library.tamu.edu/search/doc/abstract.url?SEARCHID=8247fe0cc7ca402482b58b7f1d27321a&DOCINDEX=1&database=1&pageType=quickSearch&searchtype=Quick&dedupResultCount=null&format=quickSearch&usageOrigin=compendexrefs&usageZone=compendexrefstab.
[37] List of cities by average temperature. (2020, December 27). Retrieved January 19, 2021, from https://en.wikipedia.org/wiki/List_of_cities_by_average_temperature#cite_note-NOWData_lwx-300

[38] Rattner, A. S., & Garimella, S. (2011). Energy harvesting, reuse and upgrade to reduce primary energy usage in the USA. Energy, 36(10), 6172-6183. doi:10.1016/j.energy.2011.07.047
[39] Thekdi, A., & Nimbalkar, S. U. (2015). Industrial Waste Heat Recovery - Potential Applications, Available Technologies and Crosscutting R&D Opportunities. doi:10.2172/1185778
[40] Right in the Middle: The Midwest's Growth Lessons for America. (n.d.). Retrieved January 23, 2021, from https://www.newgeography.com/content/002821-right-middle-the-midwest%E2%80%99s-growth-lessons-america
[41] U.S. energy Information administration - eia - independent statistics and analysis. (n.d.). Retrieved February 15, 2021, from https://www.eia.gov/electricity/data/browser/#/topic/0?agg=2,0,1&fuel=vvg&geo=g&sec=02&linechart=ELEC.GEN.ALL-US-97.A~ELEC.GEN.COW-US-97.A~ELEC.GEN.NG-US-97.A~ELEC.GEN.AOR-US-97.A&columnchart=ELEC.GEN.ALL-US-97.A~ELEC.GEN.COW-US-97.A~ELEC.GEN.NG-US-97.A~ELEC.GEN.AOR-US-97.A&map=ELEC.GEN.ALL-US-97.A&freq=A&ctype=map<ype=pin&rtype=s&pin=&rse=0&maptype=0
[42] U.S. energy Information administration - eia - independent statistics and analysis. (n.d.). Retrieved February 26, 2021, from https://www.eia.gov/energyexplained/biomass/
[43] U.S. energy Information administration - eia - independent statistics and analysis. (n.d.). Retrieved February 26, 2021, from https://www.eia.gov/electricity/data/browser/#/topic/0?agg=1,0,2&fuel=0008&geo=vvvvvvvvvvvvo&sec=o3g&linechart=ELEC.GEN.BIO-US-99.A&columnchart=ELEC.GEN.BIO-US-99.A&map=ELEC.GEN.BIO-US-99.A&freq=A&ctype=map<ype=pin&rtype=s&maptype=0&rse=0&pin=
[44] Wheeler, J. (2005, April 15). Geodynamics by D. L. Turcotte and G. SCHUBERT. Cambridge University Press, 2002. no. of pages: 456. ISBN 0 521 66624 4 (soft COVERS). ISBN 0 521 66186 2 (hardback). Retrieved February 26, 2021, from https://onlinelibrary.wiley.com/doi/abs/10.1002/gj.987
[45] REN21. (n.d.). RENEWABLES 2020 global status report. Retrieved February 26, 2021, from https://www.ren21.net/gsr-2020/
[46] Glassley, W. E. (2015). Geothermal energy: Renewable energy and the environment. Boca Raton, FL: CRC Press.
[47] Geothermal energy. (n.d.). Retrieved February 26, 2021, from http://butane.chem.uiuc.edu/pshapley/Environmental/L8/1.html
[48] U.S. energy Information administration - eia - independent statistics and analysis. (n.d.). Retrieved February 26, 2021, from https://www.eia.gov/electricity/data/browser/#/topic/0?agg=1,0,2&fuel=001&geo=g3g0000000ak8&sec=o3g&linechart=ELEC.GEN.GEO-US-

99.A~ELEC.GEN.GEO-NV-99.A~ELEC.GEN.GEO-CA-99.A&columnchart=ELEC.GEN.GEO-US-99.A~ELEC.GEN.GEO-NV-99.A~ELEC.GEN.GEO-CA-99.A&map=ELEC.GEN.GEO-US-99.A&freq=A&ctype=map<ype=pin&rtype=s&pin=&rse=0&maptype=0

[49] About solar energy. (n.d.). Retrieved February 26, 2021, from https://www.seia.org/initiatives/about-solar-energy

[50] Goldemberg, J., & Unidas, N. (2000). World energy assessment: Energy and the challenge of sustainability. New York, NY: United Nations Development Programme.

[51] U.S. energy Information administration - eia - independent statistics and analysis. (n.d.). Retrieved February 26, 2021, from https://www.eia.gov/electricity/data/browser/#/topic/0?agg=1,0,2&fuel=004&geo=qnifi05c03j78&sec=o3g&linechart=ELEC.GEN.SUN-US-99.A~ELEC.GEN.SUN-NV-99.A~ELEC.GEN.SUN-CA-99.A&columnchart=ELEC.GEN.SUN-US-99.A~ELEC.GEN.SUN-NV-99.A~ELEC.GEN.SUN-CA-99.A&map=ELEC.GEN.SUN-US-99.A&freq=A&ctype=map<ype=pin&rtype=s&maptype=0&rse=0&pin=

APPENDIX A

MONTHLY AND ANNUAL AVERAGE TEMPERATURE

The study considers the distribution of the average annual temperature of U.S. cities to select condenser temperatures for thermodynamic analyses. This section of the appendix lists the monthly and annual average temperature of these U.S. cities used in this study. National Weather Service Forecast Office database is referred for collecting the mean of monthly average temperatures for most U.S. cities. The annual mean temperature will predict the optimal WF for a town, while the monthly mean temperature would determine the appropriate working condition for a month. The monthly and annual mean temperatures of fifty U.S. cities are shown in Table 7 and Table 8.

Table 7. Monthly (Jan - Jun) and Annual Average Temperature in °C [37]

City	Jan	Feb	Mar	Apr	May	Jun	Year
Albuquerque	2.4	5.2	8.9	13.3	18.7	23.8	14
Anchorage	−8.3	−6.6	−3.0	2.7	8.8	12.9	2.8
Atlanta	6.4	8.6	12.6	16.7	21.3	25.2	17
Austin	10.8	12.8	16.5	20.7	24.8	27.9	20.7
Baltimore	0.8	2.4	6.8	12.4	17.6	22.8	13.1
Boise	−0.4	2.5	6.9	10.4	15.1	19.7	11.4
Boston	−1.5	0	3.7	9.1	14.6	20	10.9
Charlotte	5.1	7.2	11.3	15.8	20.3	24.7	16.1
Chicago	−4.6	−2.4	3.2	9.4	15	20.5	9.8
Dallas	7.7	9.9	14.2	18.6	23.3	27.4	19
Denver	−0.3	0.8	4.8	8.9	14.2	19.7	10.4
Detroit	−3.7	−2.3	2.7	9.4	15.2	20.7	10
El Paso	7.3	10.1	13.7	18.2	23.3	27.7	18.1
Fairbanks	−21.9	−18.3	−11.2	0.5	9.9	16	−2.3
Fresno	8.1	10.8	13.7	16.7	21.2	25.1	17.9
Houston	11.5	13.3	16.9	20.7	24.8	27.7	20.8
Indianapolis	−2.2	0.1	5.7	11.8	17.2	22.3	11.8
Jacksonville	11.7	13.6	16.5	19.4	23.4	26.7	20.3
Kansas City	−1.8	0.8	6.8	12.7	18.1	23.1	12.5

City	Jan	Feb	Mar	Apr	May	Jun	Year
Las Vegas	8.8	11.1	15	19.1	24.7	29.9	20.3
Los Angeles	14.4	14.9	15.9	17.3	18.8	20.7	18.6
Louisville	1.1	3.3	8.3	13.9	18.9	23.7	13.9
Memphis	5.2	7.5	12.2	17.2	22.1	26.4	17.2
Miami	19.9	21.1	22.4	24.2	26.5	28.1	24.9
Milwaukee	−5.2	−3.2	1.9	7.8	13.3	19.2	8.9
Minneapolis	−9.1	−6.2	0.4	8.6	15.1	20.4	7.8
Nashville	3.4	5.7	10.3	15.3	20	24.6	15.4
New Orleans	11.6	13.4	16.8	20.3	24.6	27.2	20.7
New York City	0.6	2.1	6.1	11.9	17.1	22.1	12.9
Oklahoma City	3.6	6.1	10.7	15.6	20.6	25.1	15.9
Omaha	−4.6	−2.1	4.2	10.9	16.9	22.3	10.6
Palm Springs	16.3	18.1	20.7	23.7	26.8	30.7	24.5
Philadelphia	0.5	2	6.4	12.2	17.7	22.9	13.2
Phoenix	13.6	15.4	18.5	22.7	27.8	32.7	23.9
Pittsburgh	−1.9	−0.4	4.3	10.6	15.7	20.5	10.8
Portland (OR)	5.2	6.6	8.9	11.3	14.6	17.6	12.4
Sacramento	8.1	10.6	12.7	15	18.8	22.1	16.3
Salt Lake	−1.3	1.3	6.6	10.4	15.5	21.1	11.6
San Antonio	11	13.1	16.8	20.8	25	28.1	20.8
San Diego	14.2	14.7	15.5	16.8	18.1	19.4	17.8
San Francisco	11.2	12.6	13.3	13.9	14.7	15.8	14.6
San Jose	10.8	12.5	13.8	15.2	17.8	20.2	16.4
Seattle	5.4	6.2	7.9	10.1	13.2	15.9	11.3
St. Louis	−0.1	2.4	7.9	14.1	19.3	24.4	13.9
Tampa	15.9	17.3	19.5	22.1	25.7	27.8	22.9
Tucson	11.6	13.1	15.8	19.7	24.6	29.6	20.9
Virginia Beach	4.9	6.1	9.8	14.8	19.4	24.3	15.8
Washington D.C.	2.3	3.9	8.3	13.8	18.9	24.1	14.6
Wichita	0.1	2.9	8.1	13.4	18.9	24.3	13.9

Table 8. Monthly (Jul - Dec) and Annual Average Temperature in °C [37]

City	Jul	Aug	Sep	Oct	Nov	Dec	Year
Albuquerque	25.7	24.6	20.7	14.2	7.2	2.4	14
Anchorage	14.9	13.7	9.2	1.6	−5.4	−7.2	2.8
Atlanta	26.9	26.4	23.1	17.4	12.3	7.5	17
Austin	29.4	29.9	26.7	21.8	16.1	11.4	20.7
Baltimore	25.3	24.3	20.2	13.7	8.3	2.9	13.1
Boise	24.3	23.7	18.3	11.6	4.4	−0.7	11.4
Boston	23.2	22.4	18.4	12.4	7.2	1.7	10.9
Charlotte	26.4	25.8	22.2	16.3	11.1	6.3	16.1
Chicago	23.3	22.4	18.1	11.4	4.6	−2.4	9.8
Dallas	29.7	29.8	25.6	19.8	13.7	8.4	19
Denver	23.4	22.3	17.3	10.4	3.8	−0.9	10.4
Detroit	23	22.1	17.9	11.2	5.2	−1.2	10
El Paso	28.2	27.3	24.1	18.4	11.7	7.2	18.1
Fairbanks	17.1	13.6	7.3	−4.2	−16.2	−19.8	−2.3
Fresno	28.3	27.6	24.6	19	12.4	8.1	17.9
Houston	28.9	29	26.3	21.7	16.6	12.3	20.8
Indianapolis	24.2	23.5	19.5	12.9	6.6	−0.1	11.8
Jacksonville	27.9	27.6	25.7	21.3	16.8	12.9	20.3
Kansas City	25.7	25	20.1	13.5	6.4	−0.3	12.5
Las Vegas	33.2	32.1	27.6	20.4	13.1	8.2	20.3
Los Angeles	22.9	23.5	22.8	20.3	16.9	14.2	18.6
Louisville	25.7	25.2	21.1	14.8	8.7	2.7	13.9
Memphis	28.2	27.8	24	17.8	11.8	6.4	17.2
Miami	28.8	28.9	28.2	26.4	23.7	21.2	24.9
Milwaukee	22.3	21.7	17.4	10.9	4.1	−2.9	8.9
Minneapolis	23.2	21.7	16.7	9.4	0.9	−6.8	7.8
Nashville	26.6	26.2	22.2	16	10.2	4.9	15.4
New Orleans	28.2	28.2	26.2	21.6	16.8	12.9	20.7
New York City	24.9	24.3	20.2	14.1	8.9	3.3	12.9
Oklahoma City	27.8	27.6	22.8	16.5	9.9	4.3	15.9
Omaha	24.8	23.7	18.8	11.8	3.8	−3.3	10.6
Palm Springs	33.8	33.6	30.5	24.9	19.2	15.7	24.5
Philadelphia	25.6	24.7	20.6	14.2	8.7	3	13.2
Phoenix	34.9	34.2	31.3	24.8	17.9	13.1	23.9
Pittsburgh	22.7	22	17.9	11.6	6.2	0.3	10.8
Portland (OR)	20.7	20.9	18.1	12.7	8.1	4.7	12.4
Sacramento	24.2	23.8	22.1	17.9	11.9	8	16.3
Salt Lake	26.1	25.1	19.1	11.8	4.6	−0.8	11.6
San Antonio	29.3	29.7	26.6	21.8	16.2	11.6	20.8

City	Jul	Aug	Sep	Oct	Nov	Dec	Year
San Diego	21.4	22.2	21.7	19.6	16.6	13.9	17.8
San Francisco	16.3	16.9	17.5	16.8	14.1	11.4	14.6
San Jose	21.6	21.8	20.7	17.9	13.9	10.6	16.4
Seattle	18.6	18.8	16.2	11.4	7.4	4.7	11.3
St. Louis	26.7	25.9	21.3	14.8	8.2	1.6	13.9
Tampa	28.2	28.3	27.5	24.4	20.6	17.2	22.9
Tucson	30.8	29.8	27.7	21.9	15.6	11.3	20.9
Virginia Beach	26.7	25.7	22.6	16.9	11.8	6.9	15.8
Washington D.C.	26.6	25.7	21.7	15.3	9.8	4.3	14.6
Wichita	27.3	26.7	21.7	14.6	7.4	0.9	13.9

APPENDIX B

LOW-GRADE HEAT-SOURCES

A heat-source with a temperature below 200 ˚C is considered to be a low-grade heat source. ORC is the most common method of power generation from low-grade heat-sources. There are four primary sources of low-grade heat-source. This section of the appendix addresses each source, net power harvesting potential, and its distribution in the U.S. to give the reader a clearer understanding of the energy source the authors are trying to utilize for the betterment of society.

1. INDUSTRIAL WASTE HEAT

Rattner et al. [38] found an annual generation of 613 (x106) GJ/yr of Industrial waste heat, according to the Manufacturing Energy Consumption Survey conducted by U.S. Energy Information Administration. Thekdi et al. [39], in their report, have mentioned manufacturing of chemicals, food, glass, paper, aluminum, cement, and Iron as significant contributors to waste heat generation. The industrial belt distribution in the U.S. is shown in Figure 20.

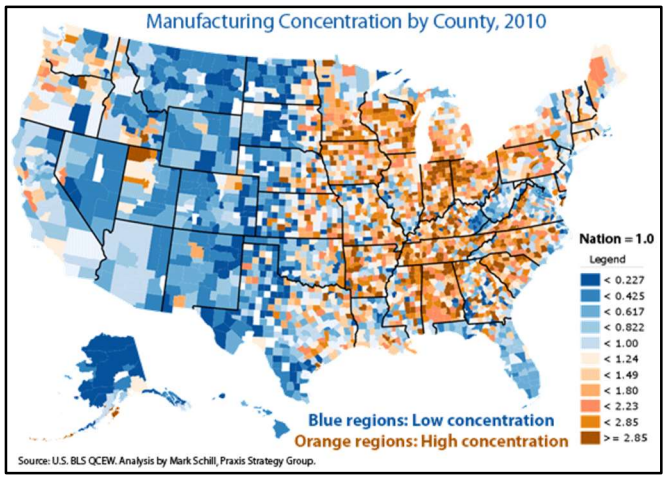

Figure 20. Distribution of Industries in the United States [40]

The Midwest and Southeast regions of the U.S. have a higher concentration of industries and are more likely to have Industrial waste heat as a heat-source for the ORC. According to EPA, in the year 2019, Texas with the maximum industrial power consumption utilized 44,579 GWh, followed by Louisiana and California, as shown in Figure 21 [41].

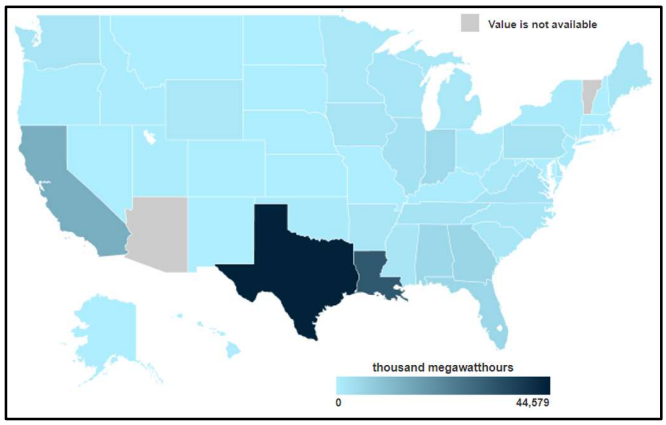

Figure 21. Industrial Power Utilization state-wise in 2019 [41]

2. BIOMASS

Biomass is renewable organic material that comes from plants and animals. Biomass was the largest source of total annual U.S. energy consumption until the mid-1800s. In 2019, biomass provided nearly five quadrillion British thermal units in the U.S., about 5% of total primary energy use [42]. The biomass energy distribution in the United States is shown in Figure 22, with California having the greatest abundance of biomass energy to be used as a heat-source for the ORC. According to EPA, in the year 2019, the state of California had the potential of harnessing almost 6,891 GWh of biomass energy, as corroborated in Figure 22.

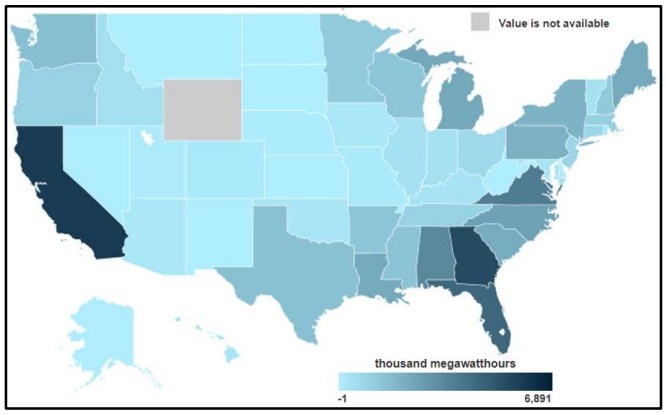

Figure 22. Biomass energy state-wise in 2019 [43]

3. GEOTHERMAL

Geothermal energy is the thermal energy generated from radioactive decay and continual heat loss from Earth's formation [44]. According to Renewables 2020 Global Status Report, in the year 2019, 13.9 GW of geothermal power was available worldwide [45]. Even though geothermal sources are cost-effective, reliable, sustainable, and environmentally friendly [46] they are limited to areas of tectonic movement like Western

U.S. states, as shown in Figure 23. In 2005, California generated 5% of its electricity from high-temperature geothermal of more than 150 °C (423.15 K) [47].

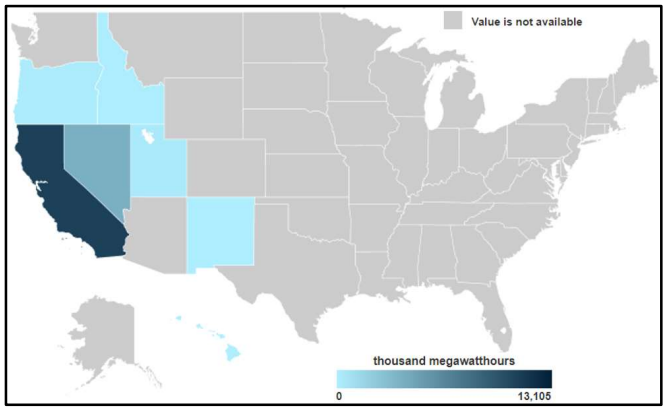

Figure 23. Geothermal energy state-wise in 2019 [48]

4. SOLAR

Solar energy is the cleanest and most abundant renewable energy source available, and the U.S. has some of the richest solar resources in the world [49]. Solar power is the solar radiation energy that is converted into thermal or electrical energy. As shown in Figure 15, in 2019, California generated close to 28.3 GWh of power by harnessing solar energy. According to World Energy Council, North America has a minimum annual solar energy potential of 181.1 Exajoules (5.03 X 107 GWh) [50] which is an enormous source of heat energy for an ORC.

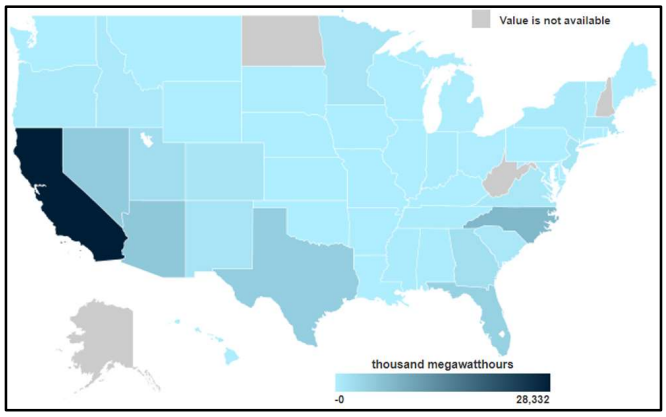

Figure 24. Solar energy state-wise in 2019 [51]

APPENDIX C

FUZZY BEHAVIOR OF DME AND DEE AT SUBCRITICAL CONDITIONS

In Section 4.1 of the study, an unusual trend was observed in Figure 7 for DME and DEE at a heat-source temperature of 400 K and 450 K. The appendix section attempts to explain the phenomenon and probable underlying reasons within the scope of this study.

Figure 7 shows the first law efficiency (η) for the WFs as a function of reduced pressure (θ) at different combinations of heat-source inlet temperatures, T_5 = 400 K, 450 K, and 500 K, and heat-sink temperature T_7 = 277 K and 300 K. The subplot area left of the vertical orange line ($\theta = 1$) in Figure 7 indicates the subcritical cycle operation. Figure 25 shows the T-s diagram for ORC, which is similar to Figure 2 discussed in the main text.

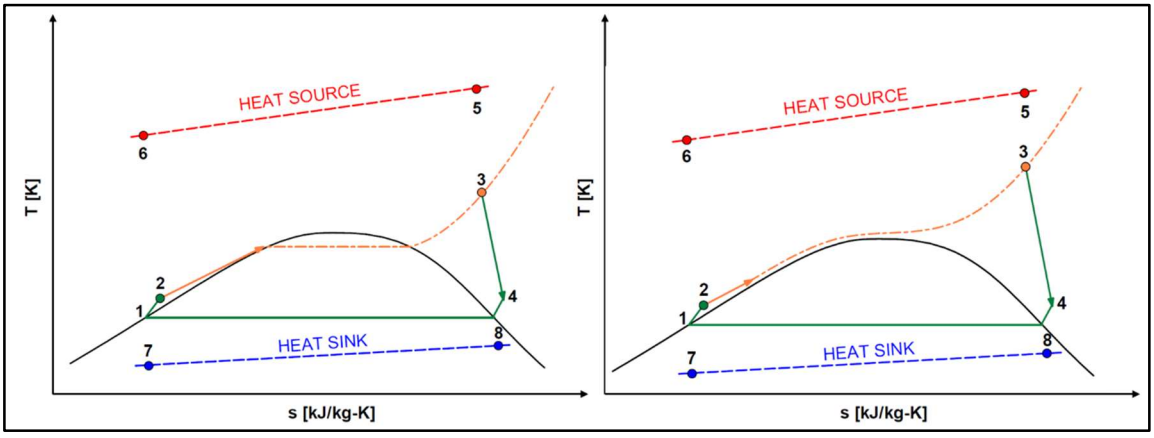

Figure 25. T-s diagram for organic Rankine cycle (left), and supercritical organic Rankine cycle (right)

At a reduced pressure of 0.84, compared to a reduced pressure of 0.83 there is a sudden 20.8% decrease in the first law efficiency of DME at a lower condenser

temperature, T_7 of 277 K, as shown in Figure 7. Similarly, at a higher condenser temperature, T_7 of 300 K, at a reduced pressure of 0.84, compared to a reduced pressure of 0.83 there is a sudden 25.1% decrease in the first law efficiency of DME. This undefined behavior is possibly the result of the closeness of critical pressures of the WFs. However, several WFs at various heat-source inlet temperatures demonstrates typical trends leading to the need for a deeper investigation.

At a lower condenser temperature of 277 K, the reduced pressure (θ) range is adjusted from half through unity with 50 data points in between for a detailed study of trends reported in Figure 8. First law efficiency (η) is the ratio of the effective work done by the cycle to the heat input to the cycle. Figure 9 investigates the variation of effective work done by the cycle with reduced pressure, and it suggests that an increase in pump work is responsible for the sudden drop in first law efficiency, as shown in Figure 7 and Figure 8 (turbine work output is constant for this study). To comprehensively analyze the undefined behavior of first law efficiency, the heat input to the cycle (Q) is also studied, and the variation with reduced pressure is shown in Figure 16. Heat input to the cycle (Q) is the heat added to the ORC from state points 2 through 3, as shown in Figure 25. Heat input to the cycle increases at the exact value of reduced pressure where there has been a drop in first law efficiency and effective work done values. First law efficiency (η) is inversely proportional to the cycle heat input for a constant effective work done; hence, an increase in the value of heat input to the cycle leads to the first law efficiency value plummeting.

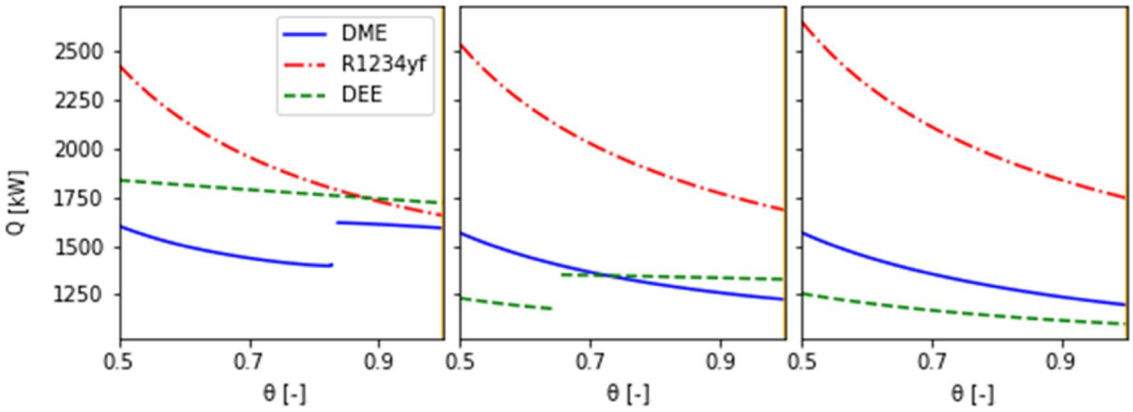

Figure 26. Variation of heat input to the cycle with θ for heat-source temperature left to the right column, T_5 = 400 K, 450 K, 500 K and heat-sink temperature, T_7 = 300 K

For both parameters, the heat input to the cycle and the effective work done by the cycle, there is dependence on the enthalpy difference in state points 3 and 4 of Figure 2. The variation of the enthalpy difference between state points 3 and 4 (Δh) and reduced pressure (θ) is given in Figure 17. As deducted earlier, Δh shows a sudden drop in values at the same values of reduced pressure. Furthermore, Δh is a function of the enthalpy at state point 3 (h_3), and the variation of h_3 and reduced pressure (θ) is shown in Figure 28. The enthalpy at state point 3 (h_3) has the same trends as all the parameters mentioned above. The enthalpy at state point 3 (h_3) is a function of the evaporator pressure (P_3) and heat-source inlet temperature (T_3), and the sudden behavior change can be finally attributed to the physical parameters of temperature and pressure that is required to maintain the work output of the turbine at a constant value. More research is required to explain this phenomenon further.

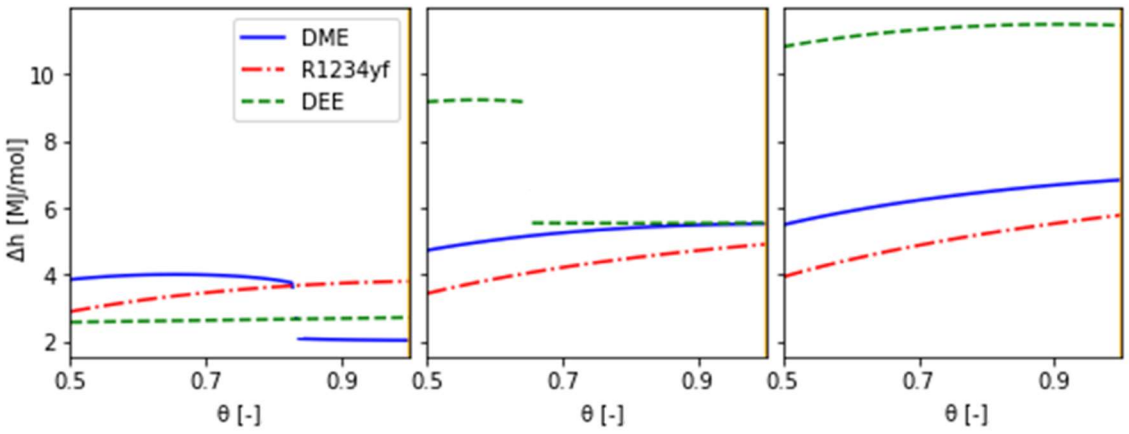

Figure 27. Variation of enthalpy difference between state point 3 and 4 with θ for heat-source temperature, left to the right column, T_5 = 400 K, 450 K, 500 K, and heat-sink temperature, T_7 = 300 K

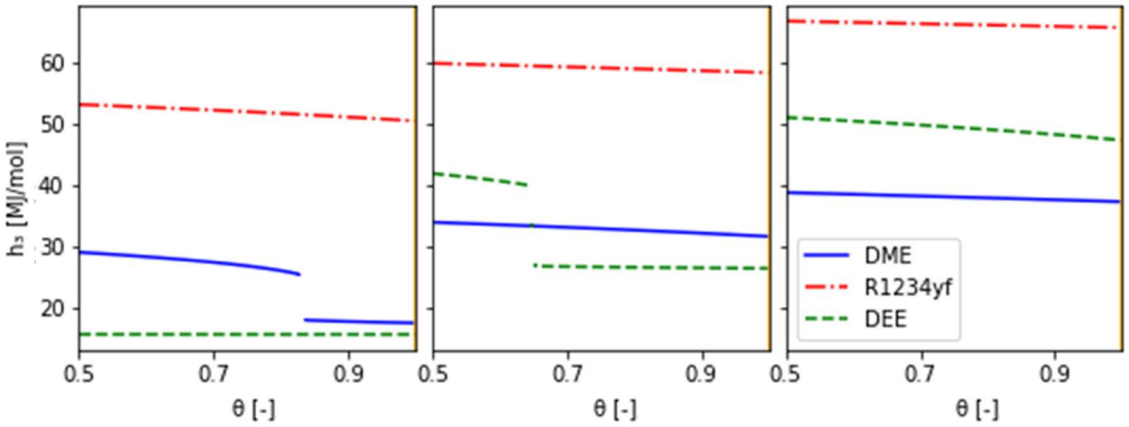

Figure 28. Variation of enthalpy at state point 3 with θ for heat-source temperature, left to the right column, T_5 = 400 K, 450 K, 500 K, and heat-sink temperature, T_7 = 300 K

Although the explanation caters to the lower condenser temperature trend, owing to a similar nature, the same reason would hold good for trends at the higher condenser temperature setting.

APPENDIX D

SCREENING OF WORKING FLUIDS

In this section, a methodology is presented and discussed that clusters fourteen WFs into families, showing similar thermodynamic characteristics for consideration in ORC applications. The method does not include complex methodologies; rather, it uses the distinguishable features in the trends of first law efficiency for screening WFs. This method has been used by Das *et al.* [20] in their study to narrow down an initial list of fourteen WFs to three for thermodynamic analyses. The initial fourteen WFs considered that were for their methodology are listed in Table 9.

Table 9. List of all working fluids and applicable properties and characteristics considered

Fluid Name	**T_c (K)**	**P_c (kPa)**	**GWP**	**Flammability**	**ASHRAE Safety Group**
Dimethyl Ether (DME)	400	5367	1	High	A3
Propene	364	4665	2	High	A3
Propane	370	4247	3.3	High	A3
R1234yf	368	3382	<1	Low	A2L
R1234ze(E)	383	3632	<1	Low	A2L
Butene	419	4005	-	-	-
Isobutene	418	4010	-	-	-
Butane	425	3796	4	High	A3
Isobutane	407	3640	3	High	A3
Diethyl Ether (DEE)	467	3644	4±2	High	A3
Pentane	470	3364	4±2	High	A3
Isopentane	460	3370	4±2	High	A3
Neopentane	434	3196	-	-	-
Novec 649	442	1869	1	-	-

The first law analysis was performed for the heat-source inlet temperatures (T_5), with the evaporator pressure ($P_2 = P_3$) being adjusted relative to the critical pressure for

each WFs. The ratio of evaporator pressure to the critical pressure of the WF, called reduced pressure (θ), varies from 0.5 to 3. Variation of first law efficiency (η) obtained against reduced pressure at a given heat-source inlet temperature is shown in Figure 29. As the source inlet temperature changes, the performance of the WFs varies with different reduced pressures relative to each other. The trends of the first law efficiency shown in Figure 29 are not interpretable, as the first law efficiency trends of many WFs overlap each other. Even so, there is a requirement for systematic screening of WFs before thermodynamic analyses to select an optimal WF.

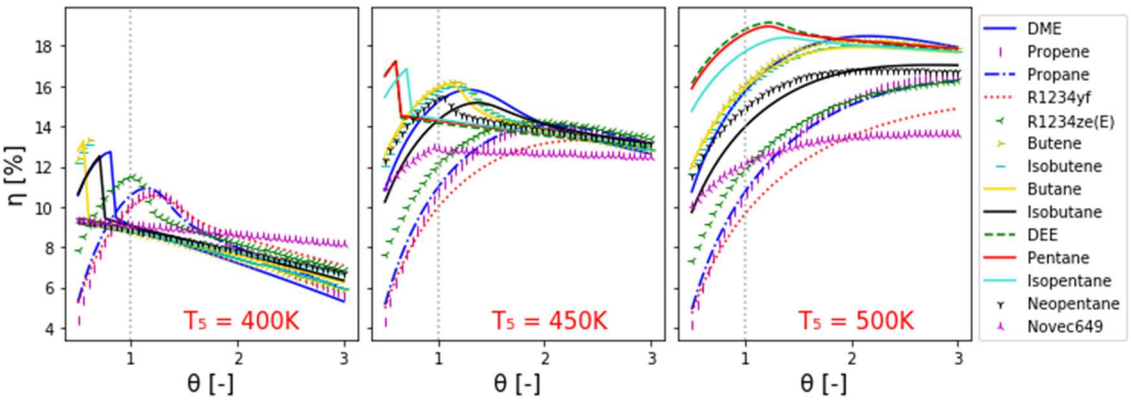

Figure 29. First law efficiency variation with θ for WFs at different heat-source temperature (T_5), heat-sink temperature (T_7) of 300 K

The screening of WFs in this study is shown for a heat-source temperature (T_5) of 400 K and heat-sink temperature (T_7) of 300 K. As shown in Figure 30, there are three notable trends of first law efficiency (η) variation with reduced pressure (θ). The first trend is where the WF exhibits a peak performance in the subcritical mode of operation. In the second characteristic trend, the WF shows a peak performance in the supercritical region

and the third observable trend, is a steady decline in efficiency with an increase in reduced pressure.

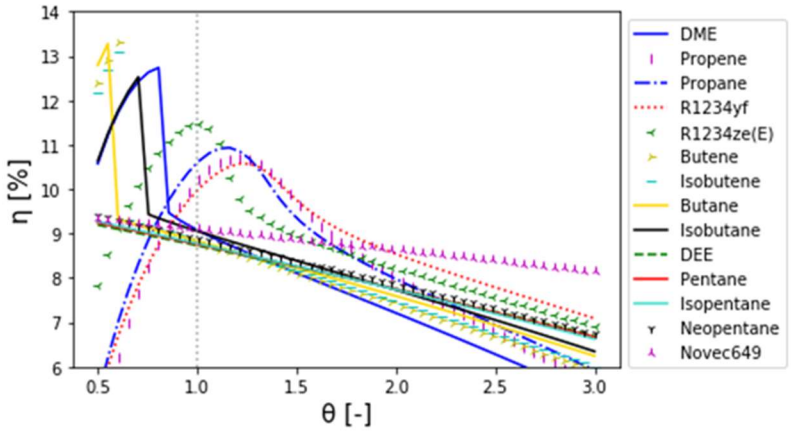

Figure 30. First law efficiency variation with θ for all WFs for T_5 = 400 K and T_7 = 300 K

A group of WFs follows the three unique characteristic trends discussed in Figure 30. Each of these trends is termed as 'Families', and the members of each family are grouped, and their first law efficiency variation with reduced pressure is shown in Figure 31. The first subplot consists of members of Family A that have a peak value in the subcritical region followed by a monotonous decrease in first law efficiency values in the supercritical region. The members of Family B, shown in the second subplot in Figure 31, have peak values in the subcritical region, followed and preceded by a slope. The last subplot with members of Family C showcases a monotonous decrease (almost linear) in first law efficiency (η) with an increase in reduced pressure (θ). Figure 31 has better interpretability compared to Figure 30, now with WFs having similar trends grouped together.

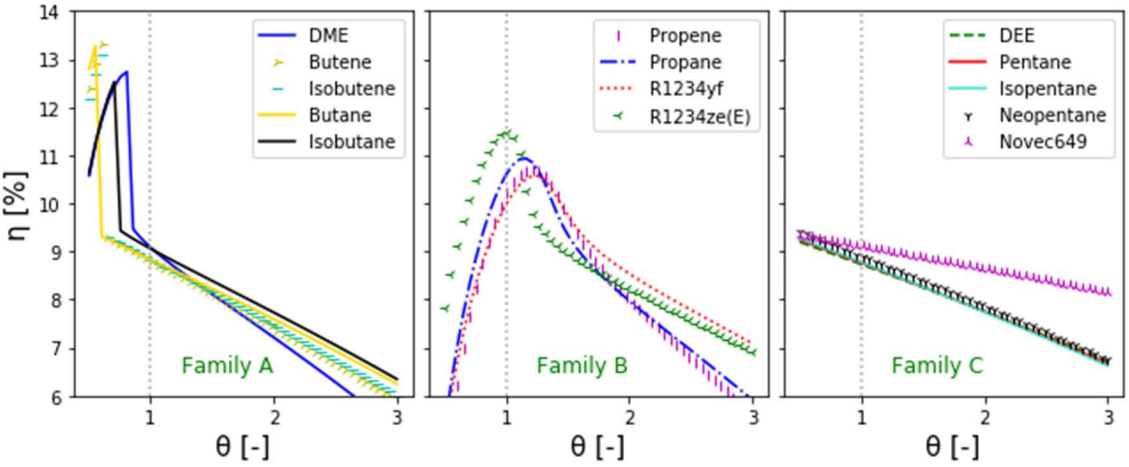

Figure 31. First law efficiency variation based on unique characteristic trends with θ for WFs at different heat-source temperatures (T_5) of 400 K and heat-sink temperature (T_7) of 300 K

As WFs, are grouped in their respective families, there are some WFs that represents, the trend of the family, better than others. In this regard, the best performing WF from each distinguishable first law efficiency trend is retained while the rest are eliminated, as shown in Figure 32. At the heat-source inlet temperature (T_5) of 400 K, DME and Butane are selected from Family A, while R1234yf and R1234ze(E) are chosen from Family B, and finally, Novec 649 is selected from Family C, all to be screened for operations at the given condition of temperature and pressure. For example, Figure 32 shows the first law efficiency variation with reduced pressure for the screened WFs.

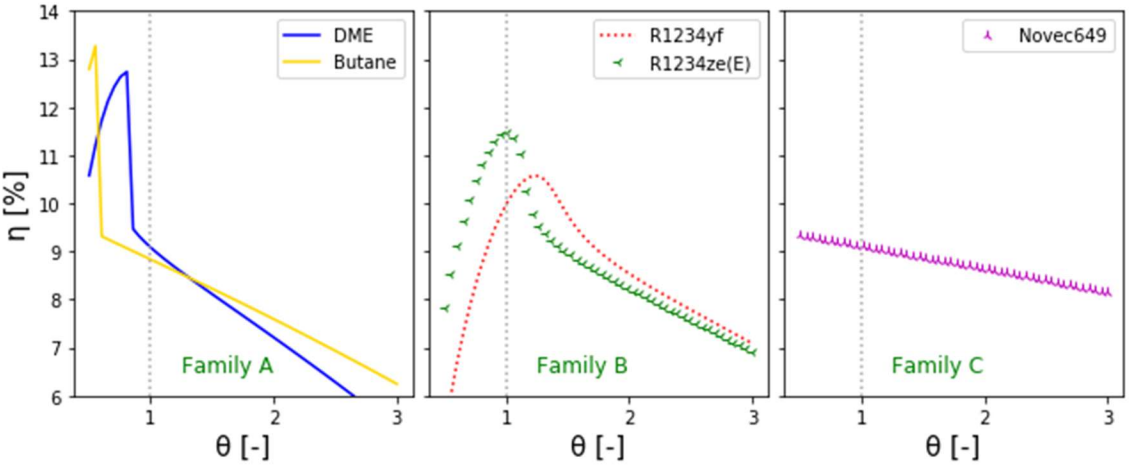

Figure 32. Distinguishable first law efficiency variation with θ for screened WFs at heat-source temperature (T_5) of 400 K and constant heat-sink temperature (T_7) of 300 K

The screened WFs from each family are condensed in a single plot shown in Figure 33 for the subsequent screening stages. Butane has the maximum first law efficiency of 13.25% at 2091 kPa (θ = 0.55); however, DME with maximum first law efficiency of 12.74% at 4302 kPa (θ = 0.81) has a better distribution of efficiency values over a range of reduced pressures. R1234ze(E) has the next highest peak, followed by R1234yf, with the latter having higher first law efficiency values in the supercritical region. Novec 649 is a synthetic WF and showcases the best performance at the given operating conditions for reduced pressure conditions of more than two. Figure 33 allows for better thermodynamic and trend interpretation than Figure 30, due to the initial screening of the fourteen WFs to five.

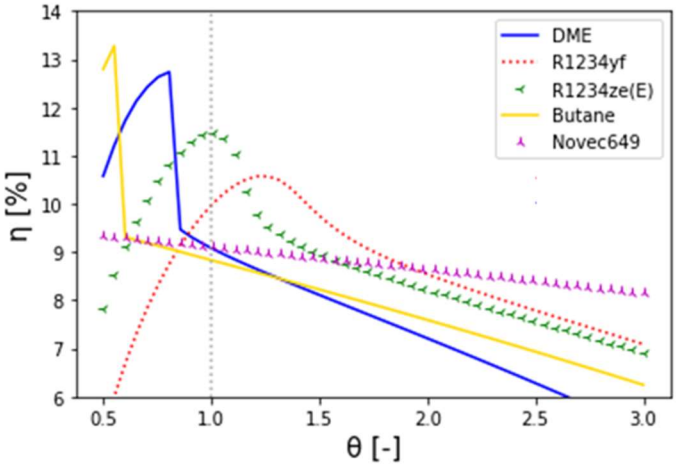

Figure 33. Distinguishable first law efficiency variation with θ for screened WFs for T_5 = 400 K and T_7 = 300 K

In Figure 34, the distinguishable first law efficiency trends shown in Figure 33 for the screened WFs are plotted against the absolute pressure scale. The plot on the left shows the variation of first law efficiency (η) in subcritical conditions against absolute pressure; similarly, the right plot showcases the variation in the supercritical state of the cycle operation. Figure 34 helps us better understand the performance of WFs and identify the WFs best suited for operation at a given temperature and pressure conditions.

Butane has a peak efficiency value of 13.25% at 2091 kPa, which is lower in pressure scale compared to peak efficiency values for DME of 12.74% at 4302 kPa. Das et al. [20] have shown in their study that lower pressure operations yield higher exergy-destruction and lower VPC, thereby eliminating butane as a WF of choice for the next phase of WF selection. Novec 649 has a lower value of first law efficiency (η) than other WFs at given pressure conditions, removing it from being an ideal choice of WF. R1234yf has lower first law efficiency values at subcritical operation but showcases better

performance than the rest of the WFs in a wide range of pressure in the supercritical mode of operation.

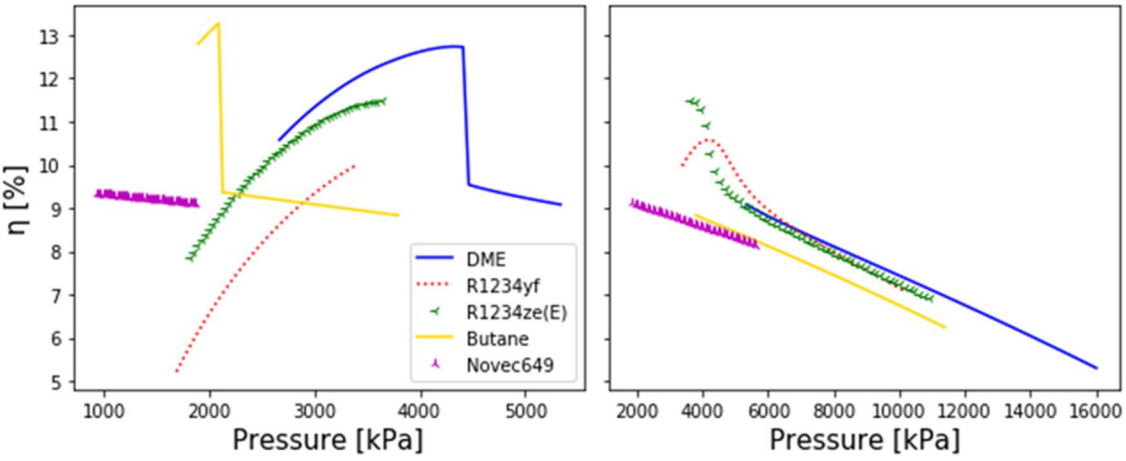

Figure 34. Distinguishable first law efficiency variation in subcritical (left) and supercritical (right) operation with absolute pressure for screened WFs for T_5 = 400 K and T_7 = 300 K

The screened WFs are next chosen for optimal performance characteristics, and the selected WFs are shown in Figure 35. DME is chosen for its peak cycle performance in the subcritical condition and R1234yf for its better first law efficiency characteristics compared to the other WFs for the rest of the reduced pressure range. DME and R1234yf are thereby chosen as WFs of choice for the operation of the cycle at a heat-source temperature (T_5) and a heat-sink temperature (T_7) of 400 K and 300 K, respectively.

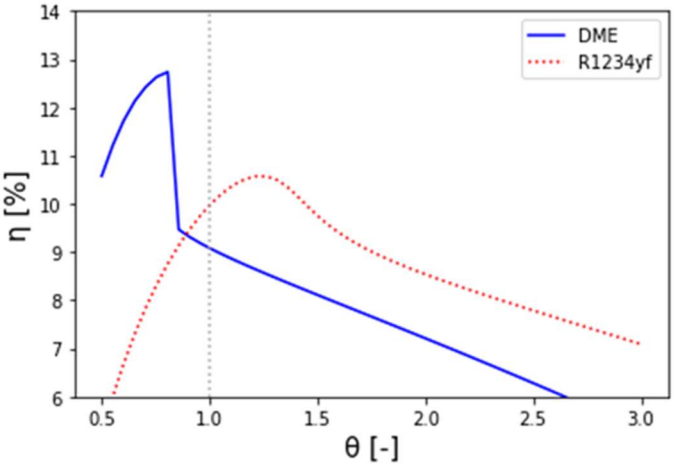

Figure 35. First law efficiency variation with reduced pressure θ for selected WFs for T_5 = 400 K and T_7 = 300 K

Screening method similar to the one carried out above for a heat-source temperature of 400 K is extended to 450 K and 500 K. As an intersection of the sets of WFs selected at each heat-source temperatures, based on categorization by family, DME & DEE are chosen as the WFs. All the eliminated WFs tend to have lower performances compared to the selected WFs. Figure 36 shows the variation of first law efficiency (η) with reduced pressure (θ) for all heat-source temperatures (T_5). These WFs have been screened and then selected to be thermodynamically analyzed for WF selection in an ORC.

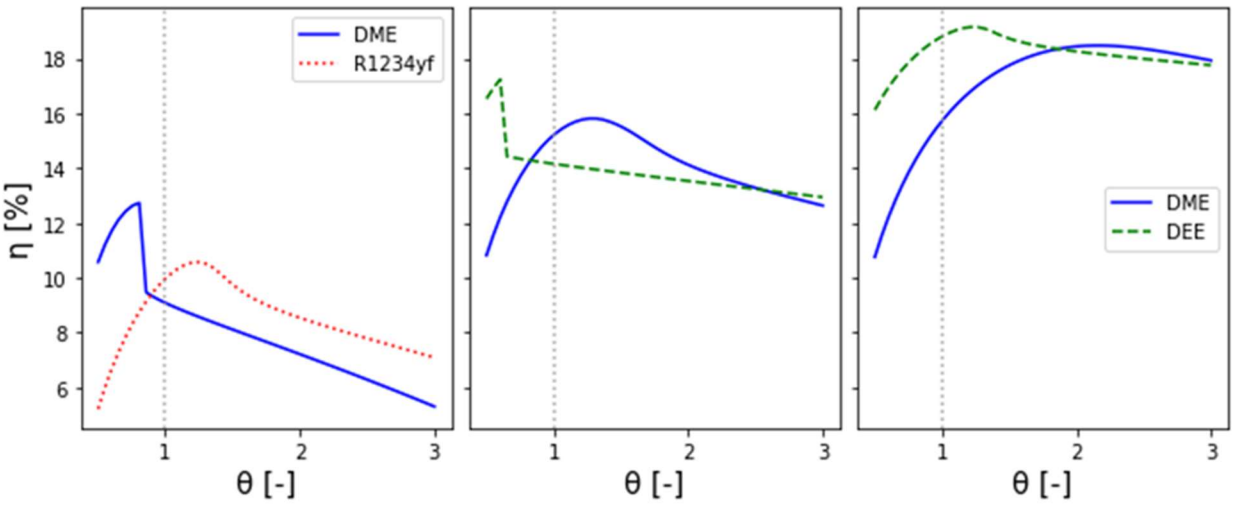

Figure 36. First law efficiency variation with θ for selected WFs at different heat-source temperature, T_5 = 400 K, 450 K, 500 K, left to the right column, and heat-sink temperature T_7 = 300 K

All the selected WFs (DME, DEE, and R1234yf) from three heat-source inlet temperatures are combined for the ORC operating at heat-source inlet temperature between 400 K and 500 K, with a heat-sink temperature of 300 K. The first law efficiency variation of the three screened WFs are shown in Figure 37. These WFs will be used in further thermodynamic analysis to select the optimal working fluid listed in Table 1.

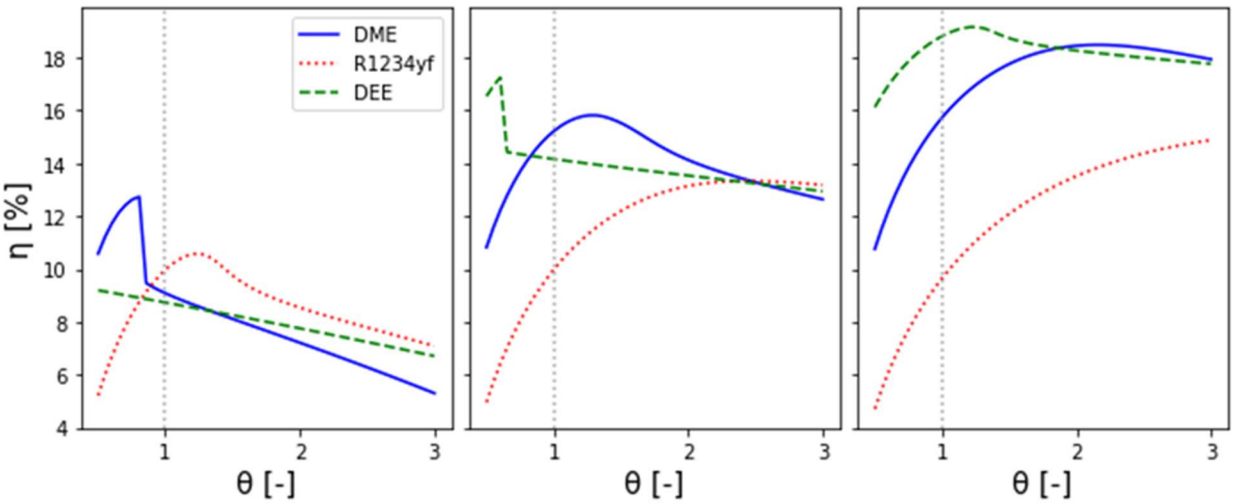

Figure 37. First law efficiency variation with θ for all selected and screened WFs at different heat-source temperature, T_5 = 400 K, 450 K, 500 K, left to the right column, and heat-sink temperature T_7 = 300 K